SAPIENZA
UNIVERSITÀ DI ROMA

Ph.D. in
Modelli matematici per l'Ingegneria, Elettromagnetismo e Nanoscienze
Curriculum di Elettromagnetismo

XXXI Cycle

Doctoral Thesis of Lorenzo Dinia

Optical Sensors for Cultural Heritage and Biomedical Applications

Supervisor
Fabrizio Frezza

Advisor
Dr. Fabio Mangini

Candidate
Ing. Lorenzo Dinia

To my aunt Lavinia, the reverence
To my uncle Mauruccio, the artlessness
To my grandma Costanza, the tenacity

1 Table of Contents

Introduction

The current Ph.D. thesis is articulated in 4 different research paths. The main research topic is on the fiber Bragg grating (FBG) sensor and its applications, mainly related to the conservation of the original status of the artworks. The second topic is related to the development of a new methodology for measuring the cracking of the Structural Health Monitoring (SHM) of cultural heritage. In the third topic, it is addressed the subject on the complex diatribe related to the risk in delivering anesthesia; field in which I have been also working, being a Biomedical Engineer. Finally, in the last topic it is proposed a biomechanics study on the patellar taping with the purpose of finding a correlation between the taping and a neuromuscular response.

A new era of pollution requires an important focus on the conservation of archaeological sites and monuments. In the last years, great efforts were made to develop various sensors for different tasks; the FBG was one of the most studied thanks to the multitude of applications and the surprising performances. An original fiber optic sensor that combines the fiber Bragg gratings with a pH responsive polymer coating for monitoring the pH of the rains on critical and prestigious monuments is proposed. In this study, the arrangement setup of the optical sensor is modeled with Comsol Multiphysics (Wave Optics Module), based on the FEM (Finite Element Method) solver. Monitoring the pH of the rain can be used by experts to predict and control the corrosion of specific materials, especially limestone and marble, thus scheduling timely restoration. This also depends on the materials under analysis and it can have an important impact in terms of cost reductions and higher maintenance efficiency. In conclusion, the swelling response of hydrogels to the change of surrounding pH allowed the development of a model of hydrogel coated FBG pH sensor. Modelling the FBG pH sensor for monitoring the rain in archaeology and in cultural heritage provided innovative results in terms of high sensitivity and small dimensions of the device, allowing better intervention planning. In the first chapter, a preliminary study regarding the optical ring resonator is conducted because, ultimately, the goal is to realize a sensor that combines the FBG and the ring resonator for future developments in order to improve the sensor performances.

Along with the development of the FBG sensor, a new methodology for measuring the cracking for the Structural Health Monitoring (SHM) of cultural heritage is also studied. The methodology is characterized by being minimally invasive on the artefact that has to be preserved, which is one of the main qualities required in this field. The approach is to determine the relative distance between two optical tags, using advanced fitting

algorithms for the objective function. Different kinds of objective-function were taken into account in order to identify the best configuration to determine the fitting parameters, useful to the SHM. The optical tags are introduced for this scope; they are nothing but adhesive labels with appropriate images, through which, by using advanced fitting methods and algorithms, it is possible to determine the absolute and relative position and three-dimensional rotations of the images.

The third chapter of this thesis deals with the risk and perception of risk in delivering anesthesia. The study examines the different perceptions of risk associated with anesthesia systems from the viewpoints of the product manufacturer and the caregiver. Only little research has been done on the impact of the perception of risk for patient safety in anesthesia. The role of the manufacturer in mitigating the perception of risk is central in the work. The risk was examined as the probability of negative occurrences based on the Medical Device Reportable (MDR) events and these risks were compared to how the caregiver perceives and manages them when delivering anesthesia. Analysis of the manufacturer's public Medical Device Reportable (MDR) events data was performed in the US market and it represents the actual risk achieved; the bibliographic review provided a perspective on how the risk is perceived and managed by the caregiver when delivering anesthesia. The goal of the research path is to highlight how the role of the manufacturers can have an impact on the reduction of perception of risk in anesthesia, increasing patient safety.

Finally, a biomechanical proposal on the estimation of Centre of Mass (CoM) trajectory has been developed. Motion capture systems and force platforms are still considered the gold standard for the estimation of accurate CoM measurements. In the last decade, several methods based on inertial sensors systems have been proposed based on double integration of acceleration signals of pelvis-worn sensors (M. J. Floor-Westerdijk, 2012). Although the portability of those methodologies is higher, drift errors due to extremely lengthy time acquisitions affect measurements, limiting their use. For the purpose of avoiding drift error and providing an accurate tool for ambulatory and/or home CoM assessment, the accuracy of a novel method based on a Biomechanical Model (BM) will be investigated. Among the large number of potential applications, this novel approach could be used in the identification of the effects of the patellar taping on neuromuscular control. More specifically, the patellar taping technique proposed by McConnell (J. McCONNELL, 1986) allows patients to engage in pain-free physical therapy exercises, by medializing the patella. Although this technique has been demonstrated to reduce the perceived pain of patients with patellofemoral pain syndrome and improve neuromuscular activity (N. Aminaka and P. A. Gribble, 2008), a deeper investigation on how patellar tape influences postural stability thought CoM assessment could be of great

interest in the long term management of Chondromalacia Patellae. It has been demonstrated, in fact, that patellar taping affects knee proprioception other than relieving pain in subjects with patellofemoral pain syndrome (M. J. Callaghan, 2008). The aim of this research program is to pursue through static and dynamic tasks performed twice both by healthy subjects and not-healthy ones, with and without patellar tape.

1. Chapter 1

Fiber Bragg Grating for pH Monitoring

1.1 Introduction

An innovative sensor for the preservation of artworks from climatic and chemical agents is central in this study. At first, the optical ring-resonator was studied and modeled. Subsequently, an original fiber optic sensor that combines the fiber Bragg gratings with a pH responsive polymer coating for monitoring the pH of the rains on critical and prestigious monuments is proposed. The goal is to combine the two principles in order to realize a miniature sensor with higher performance than the existing ones.

During the last decades, there has been a rising interest in the development of sensors based on optical fibers for several applications, including chemical sensing (M. Debliquy, 2012). Over the years, the acid rains damage monuments and other ancient artworks, destroying the historical and cultural heritage of many countries much faster. Acid rains promote the metal and marble corrosion and the destruction of monuments resulting in loss of mechanical strength and compactness, causing a partial dissolution of the materials themselves (R.J. Cheng, 1987). The sulfates, present in the acid rain, transform the calcium carbonate into gypsum, known as soft sulfate mineral composed of calcium sulfate dehydrate (R.J. Cheng, 1987). This phenomenon is very critical in countries like China because of the tremendous pollution that started with the fast industrial growth of the past years, which triggered an acceleration in the destruction of buildings and artworks (R.J. Cheng, 1987). This has created in the last years a growing interest on how to identify the starting point of the damages for preventing them (A. Singh, 2008). In the past, optical analysis and analytical techniques have been used to identify the material responsible for the corrosion and deterioration of the original artworks' material, discovering that the gypsum was always present in samples of deteriorated marble (R.J. Cheng, 1987). Moreover, traces of nitrates and sulfates were investigated on marble

surfaces' samples. It was discovered that although both sulfates and nitrates are elements present in the acid rain in significant quantities, the concentration of sulfates on the samples was 20 times bigger than the quantity of nitrates (R.J. Cheng, 1987). This result provided a significant indication about the leading responsibility of the sulfates in deteriorating marbles (R.J. Cheng, 1987).

The problem of the acidification of the air and rains was discussed and addressed many years ago during the Medieval Era, even if it was limited to few compounds mainly released around the cities and to the volcanic eruptions (D. Camuffo, 1992). Acid rain has been detected, during the second half of the nineteenth century, primarily in Europe, East Asia and North America (A. Singh, 2008). The industrial age improved the average life quality of human beings but on the other hand provoked intense atmospheric acid deposition through rain, fog, and snow, threatening the environmental stability and the conservation of monuments and artworks (A. Singh, 2008).

The corrosion of different materials cannot be prevented without continuously monitoring the pH of the rain. Nowadays, the catastrophic effects of the polluted rains are addressed merely with restoration after visible damages, such as micro-cracks, discoloration, and corrosion as shown in Figure 1.

Figure 1. Fountain of the Obelisk of Republic Square - Fondi (LT), Italy.

1.2 Acidity of the Rain – Enemy for the Artworks

The main enemy of the artworks is the acidity of the rain, (A. Singh, 2008; G.E. Likens, 2008) that attacks the statues and ancient buildings, causing enormous damages without

control. The calcareous building stones are among materials one of the most sensitive to pollutants (R. Butlin, 1990; S.J. Haneef, 1992). Normal rain is not neutral like pure water but is slightly acidic at around 5.6 pH or lower (A. Singh, 2008; G.E. Likens, 2008). Industrial areas have registered acidity of the rain below a pH value of 2.4 (A. Singh, 2008; G.E. Likens, 2008). Rainwater becomes weakly acidic because carbon dioxide gas in the atmosphere reacts with water to form carbonic acid. Moreover, the rainwater increases the acidity even more, mixing with sulphur oxide and nitrogen oxide molecules, because of industrial pollution and automobile exhaust (R.J. Cheng, 1987; A. Singh, 2008; G.E. Likens, 2008; R. Butlin, 1990; S.J. Haneef, 1992). The corrosion rate on artworks is much faster in industrialized areas and areas where human activities are more intense (A. Singh, 2008; D. Camuffo, 1992). Sand stone, limestone and marble of monuments and artworks are affected by acid rain because calcium carbonate, one of the main constituents of these materials, reacts with sulphur, present in dry deposition, and form calcium sulphate (A. Singh, 2008; R. Butlin, 1990; S.J. Haneef, 1992). This product is very soluble and all the acids formed thereby and deposited are washed off the stone's surface with the following rains, damaging the world's cultural heritage, ancient monuments, historic buildings, sculptures, and paintings (A. Singh, 2008). Therefore, acid rains are responsible for the loss of original features and the impairment of monuments and artworks (A. Singh, 2008; R. Butlin, 1990).

The different sources of SO_2 emissions are the burning of coal and petroleum, several industrial processes, the smelting of iron and some other metals, the manufacturing of sulphuric acid, and all the activities related to the acid concentrators in the petroleum industries (A. Singh, 2008; R. Butlin, 1990; S.J. Haneef, 1992). Surely, the emission of NO_x, compared to SO_2, are much less but still harmful in making the rain even more acidic (A. Singh, 2008; R. Butlin, 1990; S.J. Haneef, 1992). There are natural sources of nitric oxide but men contribute heavily with power plants, vehicle exhausts, and industrial processes too (A. Singh, 2008; R. Butlin, 1990; S.J. Haneef, 1992).

In this scenario, in which the sustainability is one of the main objectives of the industrialized countries, monitoring the damages caused by the pollution is necessary for improving the quality of human life, reducing diseases as well as for economic reasons. With an innovative monitoring procedure of the pH of the water, maintenance and restoration programs can easily be set depending on the chemical features of the rains over the years.

1.3 Optical Ring-Resonators

In the last two decades, on-chip label-free biochemical sensors have attracted a lot of attention from many researches thanks to their small footprint and high sensitivity (X. Fan, 2008; S. Roh, 2011). The miniaturization of sensors is one of the main features for lab-on-chip sensing applications, considering that a small amount of analyte (antigens, proteins, biotin, and aminoacids) is needed to accomplish the analysis. The miniature sensors can be organized in arrays, in these multiple configurations it is possible to increase the sensitivity and also to sense different analytes, simultaneously.

The dielectric microresonators are characterized by very high quality-factors (Q-factors) with very sharp resonance line-shapes, which are used to detect a small environment refractive index change (L. Zhou, 2011). Mainly, the microresonators have the optical energy localized in the dielectric core and only a very small amount of energy is transmitted, as evanescent field, outside in the dielectric cladding, which ultimately limits their sensitivity (L. Zhou, 2011). One of the most important factors for an optical ring resonator is to find a tradeoff between reducing waveguide dimensions or using slot waveguide structures in the microring resonators for improving the sensitivity (C.F. Carlborg, 2009; T. Claes, 2009) and a quite large bending radius to maintain a low loss thanks to the low optical confinement of the waveguide (L. Zhou, 2011).

During the study, it was conducted an evaluation on different optical O-Ring resonator geometries. The goal was to find the geometry that optimized the structural parameters for identifying the highest refractive index sensitivity. The range of refractive indices between 1.2 and 1.54 has been considered during the study for the biological material to detect. It was assumed a magnetic permittivity μ equal to 1 and a conductibility σ equal to 0 for the entire geometry. The inefficiency of conductive capacitors in detecting chemical substances was taken in consideration and, thus, the null conductivity for the whole structure was set.

The optical ring resonator consists of a straight waveguide and a ring waveguide close to each other, so light couples from one waveguide to the other. The resonance is reached when the length of the ring waveguide is an integer number 2π of wavelengths. When this happens, the light power stored in the ring builds up. The wave transmitted through the straight waveguide is the interference of the incident wave and the wave that couples over from the ring to the straight waveguide (Comsol Application License 5.2). The confinement of the energy in the core of the ring is described by the Whispering Gallery Mode; the EM waves circulate and are strongly confined within the structure (G. C. Righini, 2011).

Along the study and the different simulations, it has been discovered that if the core of the waveguides increases, then the single mode propagation moves to a multimode condition, with high interference in the propagation (R. Gotti, 2013). Reducing the bending radius of the O-Ring causes also an increase of multimodality (R. Gotti, 2013).

1.3.1 The Basic Configuration of the Single Ring Resonator

A ring resonator is made of a straight guide and an O-ring as showed in Figure 2.

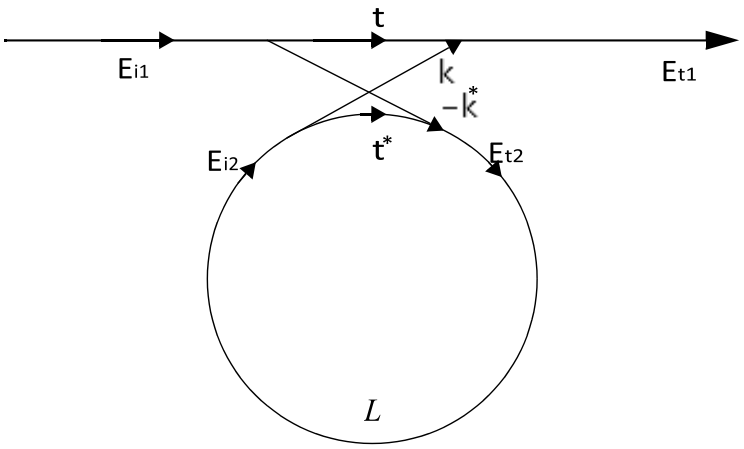

Figure 2. Schematic of an optical ring resonator, showing the incident fields Ei1 and Ei2 and the transmitted/coupled fields Et1 and Et2. The transmission and coupling coefficients t and κ are also indicated, as well as the round-trip loss L.

When a single unidirectional mode of the resonator is excited, the coupling is lossless, single polarization is considered, none of the waveguide segments and coupler elements couple the waves of different polarization, all the losses occurring along the propagation of light in the ring resonator filter are incorporated in the attenuation constant L. The interaction between the straight waveguide and the ring waveguide can be described by the matrix relation,

$$\begin{pmatrix} E_{t1} \\ E_{t2} \end{pmatrix} = \begin{pmatrix} t & k \\ -k^* & t^* \end{pmatrix} \begin{pmatrix} E_{i1} \\ E_{i2} \end{pmatrix} \qquad (1.1)$$

The coupler parameters *t* and k depend on the specific coupling mechanism used. The $*$ denotes the conjugated complex value of t and κ, respectively. The matrix is symmetric because the networks under consideration are reciprocal. The matrix above defines an equality between the input power and the output power according to the relation,

$$|E_{t1}|^2 + |E_{t2}|^2 = |E_{i1}|^2 + |E_{i2}|^2 \quad (1.2)$$

The relationship between the coupling and transmission coefficients is

$$|t|^2 + |k|^2 = 1 \quad (1.3)$$

To simplify the model even more the E_{i1} is chosen to be equal to 1; then the waveguide that propagates around the ring waveguide can be expressed by,

$${E_{i2}}^2 = L \cdot {E_{t2}}^2 \cdot e^{j\theta} \quad (1.4)$$

where *L* is the loss coefficient of the ring (zero loss: $L = 1$) and $\theta = \omega L/c$, L being the circumference of the ring which is given by $L = 2\pi r$, r being the radius of the ring measured from the center of the ring to the center of the waveguide, *c* the phase velocity of the ring mode ($c = c_0/n_{eff}$) and the fixed angular frequency $\omega = kc_0$, c_0 refers to the vacuum speed of light. The vacuum wavenumber *k* and the wavelength λ are linked through: $k = \frac{2\pi}{\lambda}$ (D.G. Rabus, 2007). Using the vacuum wavenumber, the effective refractive index n_{eff} can be introduced into the ring coupling relations by

$$\beta = k \cdot n_{eff} = \frac{2\pi \cdot n_{eff}}{\lambda} \quad (1.5)$$

where β is the propagation constant. From the prior relationship,

$$\theta = \frac{\omega L}{c} = \frac{kc_0 L}{c} = k \cdot n_{eff} \cdot 2\pi r = \frac{2\pi \cdot n_{eff} \cdot 2\pi r}{\lambda} = 4\pi^2 \cdot n_{eff} \frac{r}{\lambda} \quad (1.6)$$

From the equations (1.1) and (1.3) the values E_{i2}, E_{t1} and E_{t2} can be obtained (D.G. Rabus, 2007). These three values are used to determine the transmission power P_{t1} in the output waveguide,

$$P_{t1} = |E_{t1}|^2 = \frac{L^2 + |t|^2 - 2L|t|\, cos(\theta + \varphi_t)}{1 + L^2|t|^2 - 2L|t|\, cos(\theta + \varphi_t)} \quad (1.7)$$

where $|t|$ is the transmission loss and φ_t the corresponding phase of the coupler.

$$t = |t| \cdot e^{-j\varphi_t} \quad (1.8)$$

The power that circulates in the O-ring is given by,

$$P_{i2} = |E_{i2}|^2 = \frac{L^2(1-|t|^2)}{1+L^2|t|^2-2L|t|\,cos(\theta+\varphi_t)} \quad (1.9)$$

When the resonance is reached for $(\theta+\varphi_t)=2\pi m$, where *m* is an integer, the two following equations are obtained,

$$P_{t1} = |E_{t1}|^2 = \frac{(L-|t|)^2}{(1-L|t|)^2} \quad (1.10)$$

$$P_{i2} = |E_{i2}|^2 = \frac{L^2(1-|t|)^2}{(1-L|t|)^2} \quad (1.11)$$

1.3.2 Simulation of Different Device Configurations

An interesting case happens for $L=|t|$ in (1.10), that is, the internal losses are equal to the coupling losses, in this scenario the transmitted power is 0. This is a known result due to critical coupling, consequence of destructive interference.

Figure 3 shows the model's geometry based on a straight waveguide and a ring waveguide. Because it is expensive and time consuming to try to optimize the design configuration for an optical ring resonator with an experimental approach, the device is modeled through Comsol Multiphysics (Wave Optics Module), based on the FEM (Finite Element Method) solver. The cladding is set an order of magnitude greater than the core. The distance between the two waveguides is changed during the study in order to optimize the coupling. This last parameter has been investigated deeply because it does not exist an optimal distance between the waveguides for the entire spectrum of refractive indices. The simulation is the most efficient way to better understand the evanescent coupling for different design of resonators (H.K. Cho, 2012).

The sensing characteristics of such structure are, systematically, analyzed by investigating the transmission spectrum. This research is focused on the geometries that show the highest sensitivity. The study starts with the basic optical O-Ring resonator and, then, several variants of the initial geometry are proposed and analyzed. The parameters used for the simulation are shown in Table 1.

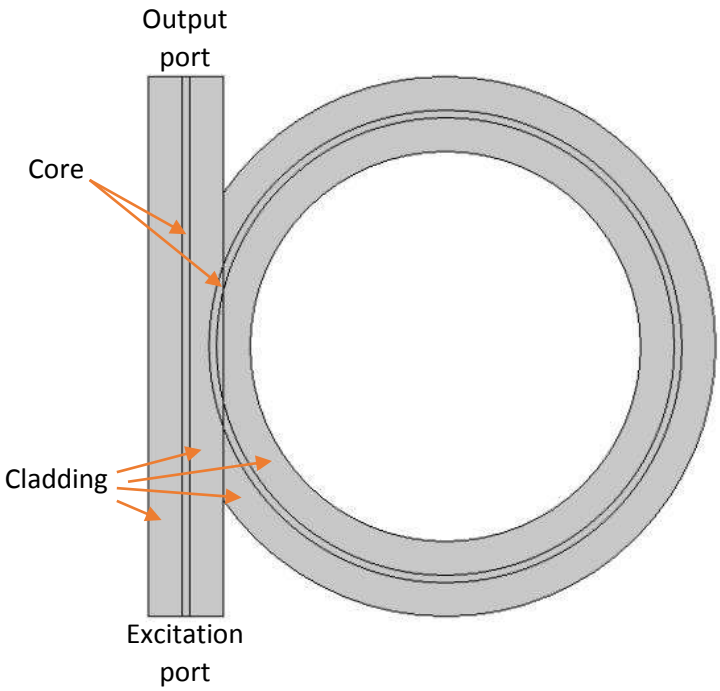

Figure 3. Starting model's geometry.

Table 1. Initial parameters used for the simulation with relative numerical values and descriptions.

Parameter	Numerical Value	Description
w_{l0}	1.55[µm]	Initial wavelength
w_l	w_{l0}	Wavelength
f_0	c_const/w_l	Frequency
w_core	0.2[µm]	Core width
w_clad	10*w_core	Cladding width
r_0	4*w_{l0}	Radius of curvature
n_core	2.5	Core refractive index
n_clad	1.5	Cladding refractive index
dx	3.5833*w_core	Separation between waveguides

Figure 4 shows the transmittance spectrum. This model reaches the resonance condition, which is when the transmittance is approximately null, for wavelength equal to 1.560 x 310 $^{-6}$ [m] with core's refractive index 2.5 and cladding's refractive index 1.5.

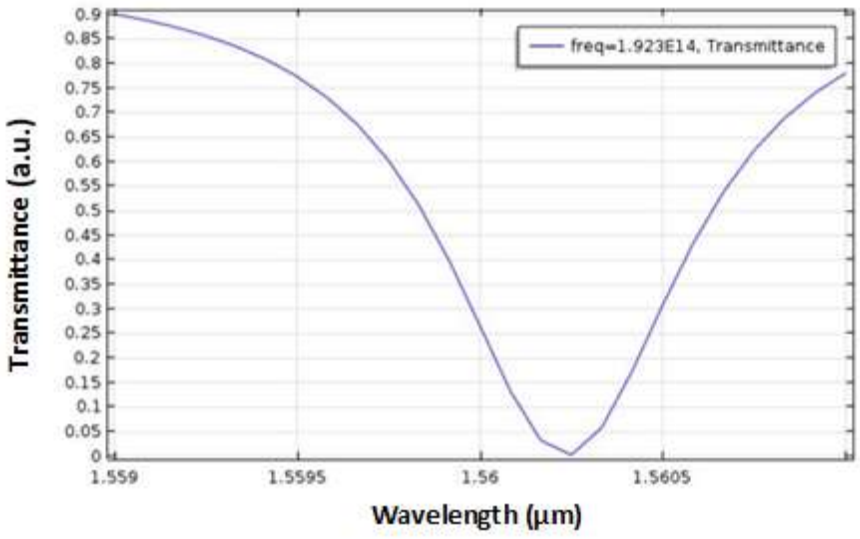

Figure 4. Transmittance spectrum for the optical ring resonator with core's refractive index 2.5 and cladding's refractive index 1.5.

Figure 5 shows the *Z* component of the Electric field for the resonance wavelength. The field in the straight waveguide and the field incoming from the ring are out-of-phase when they interfere in the coupler. Because of that, the outgoing field in the straight waveguide on the output port is almost zero. The mono modality condition is also visible.

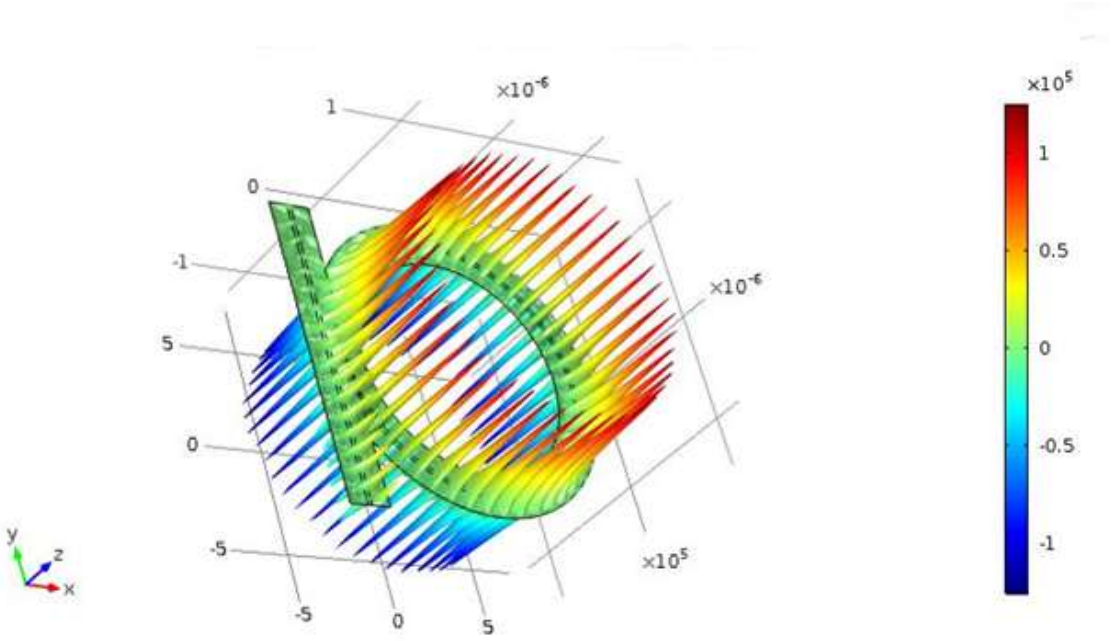

Figure 5. The out-of-plane component of the electric field [V/m] for the resonant wavelength.

In Figure 6, the transmittance spectrum changed compared to Figure 4 due to the cladding refractive index set to 1.2. The resonance shifted from 1.5603 [µm] to 1.6078 [µm]. The propagation of the electromagnetic field is still a single mode because no geometrical changes were made. A higher electrical field propagating around the ring was also noticed compared to the previous case.

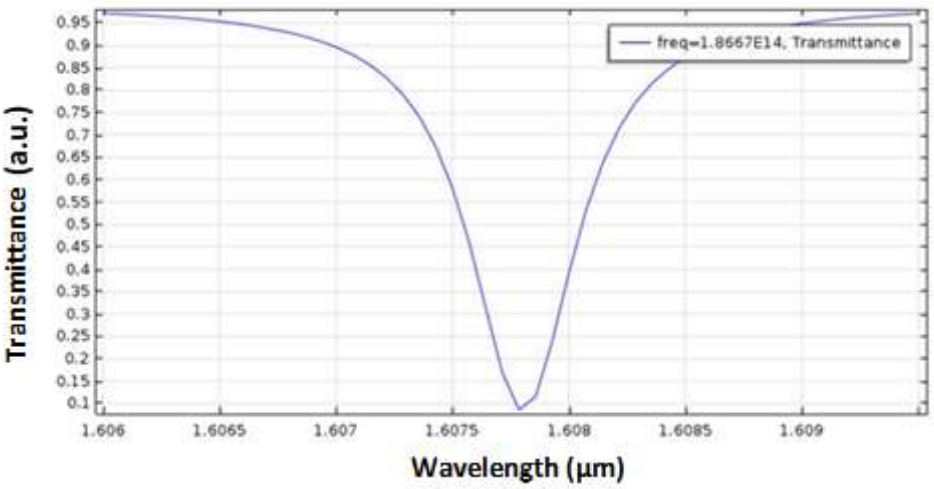

Figure 6. Transmittance spectrum for the optical ring resonator with core's refractive index 2.5 and cladding's refractive index 1.2, dx = 0.71666 µm. Resonance at 1.6078 µm.

The initial geometry of Figure 3 was modified, inserting an additional material inside the O-Ring; a full O-Ring (Figure 7) was created. A second variant with an extra layer was considered, inserting it right next to the internal cladding of the O-Ring as shown in Figure 9. In these two different scenarios, the whispering gallery mode principle was overlooked. The only small differences with the first model were a slightly higher multimodality and a slightly lower field intensity.

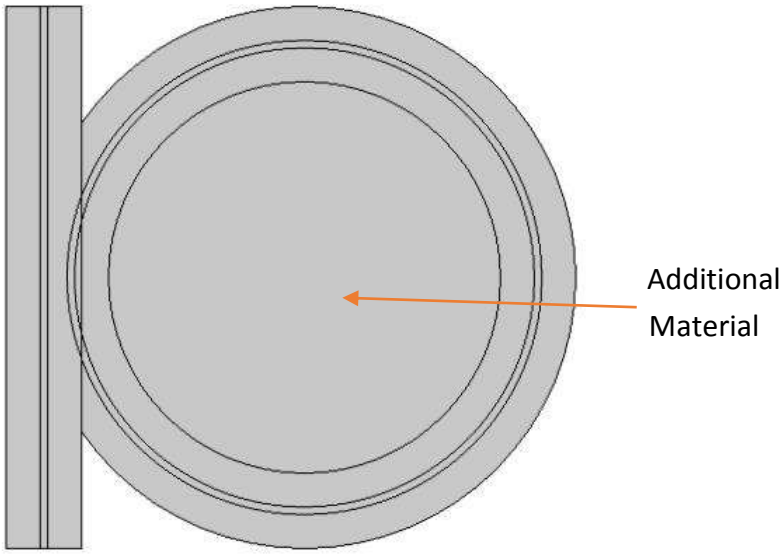

Figure 7. Model's geometry with full Ring.

With the Full O-Ring model no relevant outcomes were obtained. The presence of the full ring does not affect the transmittance on the straight waveguide as expected. This can be explained with the whispering gallery modes theory. This specific mode is characteristic to the bent waveguide curve and it is reached by increasing the core of the bent guide. When the whispering mode condition is reached, the modes are guided only from the external dielectric interface, causing the internal interfaces to be irrelevant (R. Gotti, 2013). For the first-order resonance the electrical field and the high radiation intensity exist inside the periphery of the ring, for the second-order resonance, there are two glittering loops inside the O-Ring. The inner loop is higher than the outer one, therefore, it may be preferred in sensing applications thanks to the stronger interactions with the material in proximity to the inner boundary of the ring through the evanescent field (H.K. Cho, 2012).

It is very interesting to underline that for harmonics higher than the first, the propagation has an increasing in multimodality, a shift of the maximum peak of intensity, a wider radial profile of the EM field and a higher external field (R. Gotti, 2013). An important result is to reach the mono modality, relevant factor during the coupling between the two guides, because better confinement of the field and higher intensity peak are reached in proximity to the external interface.

In Figure 8, it can be noticed the step per each frequency for the three refractive indices studied 1.25, 1.45 and 1.65. The variation on the transmittance spectrum for the three refractive indices is very small, suggesting a very small sensitivity of the model.

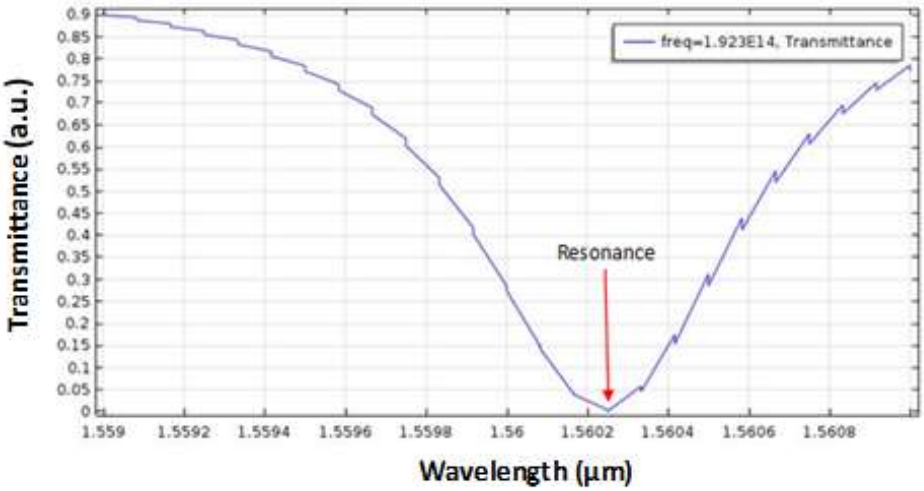

Figure 8. Transmittance spectrum for the optical full ring resonator. In the frequency spectrum between 1.559 and 1.561 µm the refractive indexes 1.25, 1.45, 1.65 are shown for each frequency.

To improve the model a geometry (Figure 9) with an extra internal circular crown compared to the geometry in Figure 3 has been proposed.

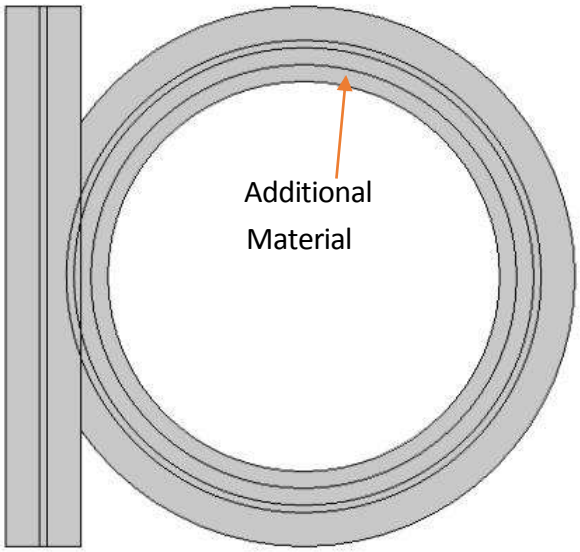

Figure 9. Model's geometry with additional crown inside the O-Ring.

For this model the same issue of the model with the full Ring was encountered. The internal layers of the O-Ring are irrelevant for the propagation of the electromagnetic field. Several combinations of distances (dx) between the waveguides, various waveguides lengths and refractive indices for the additional material have been studied.

From the results of the simulations a high multimodality and a high interference among modes were noticed. The results suggested that the O-Ring resonator is highly dependent on the material of the system and less dependent on geometrical characteristics. Varying the refractive index either of the core or of the cladding on the geometry drastically changed the results.

The model has been studied with a refractive index of the internal layer of the O-Ring equal to 1.33. Figure 10 shows the transmittance spectrum. It shows a behavior similar to the transmittance spectrum of Figure 4, but with lower sensitivity because of the multimodality mode and, thus, the loss. The system reaches the resonance condition for wavelength equal to 1.7239 e-6 µm with core's refractive index 2.5 and cladding's refractive index 1.5. Even when the resonance condition is reached the transmittance is still close to 0.35.

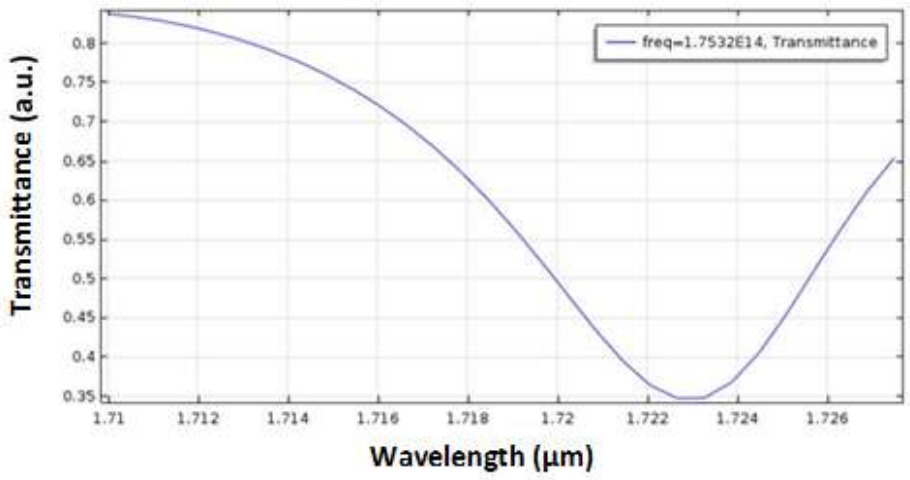

Figure 10. Transmittance spectrum for the optical ring resonator with core's refractive index 2.5, cladding's refractive index 1.5, and the extra crown's refractive index 1.33.

In a further simulation, the additional material was inserted, internally, in contact with the core of the O-Ring as shown in Figure 11, the internal layer of cladding was removed. The thickness of the internal layer is half of the thickness of the cladding's external layer. The model has also been studied varying the parameter *dx* in the range between 0.675 and 0.7125 µm and the wavelength in the range between 1.5 and 1.7125 µm. No interesting sensing properties have been identified with this geometry.

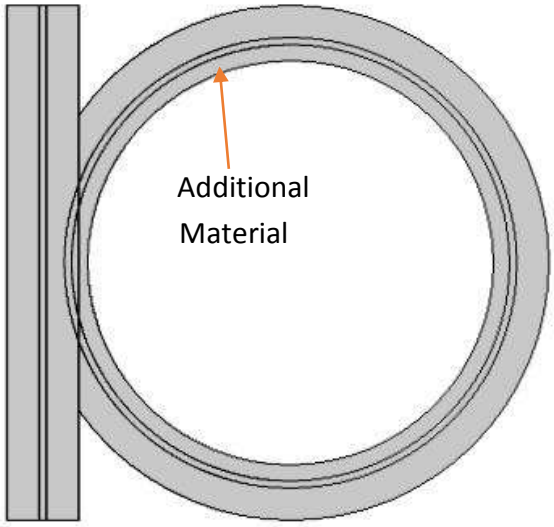

Figure 11. Model's geometry with additional crown inside the O-Ring, without the cladding internal to the Ring.

The results of the simulation show a very low variation of the propagation within the wavelengths range of 1.626 - 1.63 µm for dx equal to 0.6875. The simulation has been run for the entire combinations of the two parameters under study and it has been obtained a very low dependency both from geometrical parameters and from the material.

The coupling between a straight waveguide and a ring waveguide is based on a variant of the coupling modes (R. Gotti, 2013). The following Figure 12 shows the coupling rectangular region, highlighted in violet, which is considered in the next analysis. Within that area, the optical field can be represented by a linear combination of the modes of the straight and of the ring waveguides (R. Gotti, 2013). The description of the coupling between the two waveguides is based on a variant of the theory of the coupling modes.

The electric and magnetic fields are described by the scattering matrix *S*, obtained considering the orthogonal condition among the modes and a field approximately null outside the region.

$$S = Q \times T \times P^{-1} \tag{1.12}$$

Where the matrices Q and P are specific diagonal matrices containing the exponential terms. These are function of the propagation's constants for the modes, of the radial and angular coordinates for the ring waveguide, and of the spatial coordinate for the straight waveguide (R. Gotti, 2013).

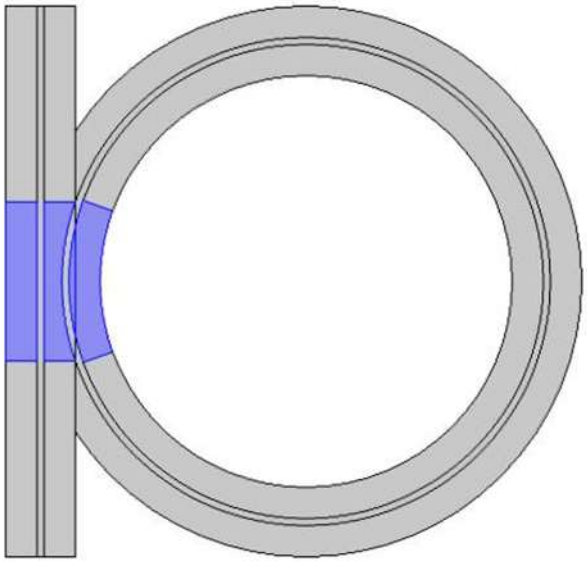

Figure 12. O-Ring Resonator with the coupling rectangular region identified by the violet area.

Figure 13 indicates the existence of three resonance peaks in the transmission spectrum in the frequency range of 1.53 – 1.67 µm. The relationship between the refractive index of the substance in the coupling region and the peaks of the transmittance spectrum is mostly nonlinear. The transmission spectrum of Figure 13 shows nonlinear characteristics for different refractive indices from 1.38 to 1.52 with step of 0.02 in the wavelength range. From an analysis of the shift of the peaks for the different refractive indices, it can be noticed a sensitivity, defined as $\frac{d\lambda}{dn}$, not higher than 150 nmRIU^{-1}. Because of the low sensitivity and high non linearity of the system, an optimization process has to be adopted in order to achieve a higher sensitivity and a linear relationships, changing the structural parameters of the sensor. A smaller range could be studied, i.e. between 1.58 and 1.62, in order to determine the behavior of the specific type of material to a certain frequency for various structure's configurations.

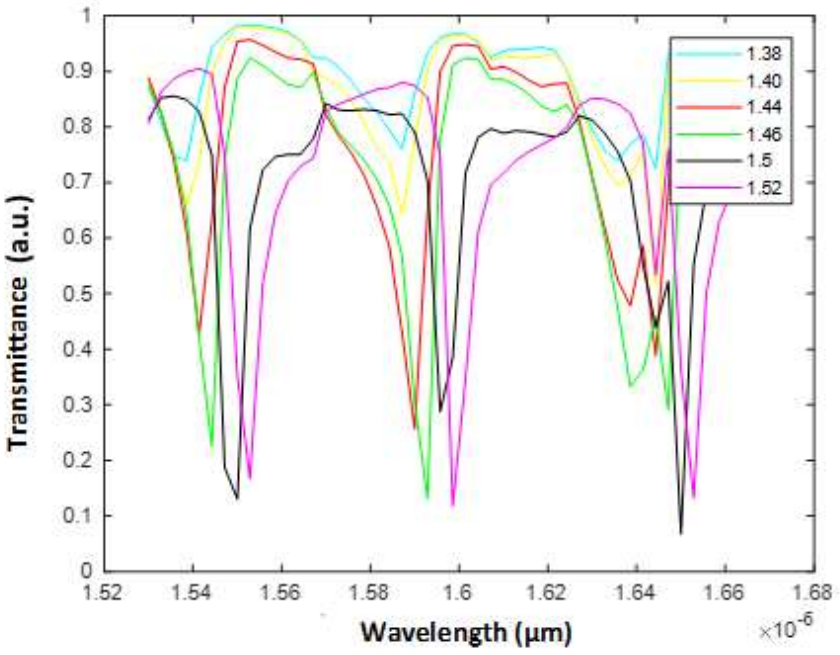

Figure 13. The transmission spectrum of the structure for refractive indices 1.38, 1.4, 1.44, 1.46, 1.5, 1.52, respectively.

Sensitivity is the key parameter to characterize sensor performance. The focus is to reach the highest sensitivity with small dimensions and low loss for the sensor (T. Wu, 2014). The resonant frequencies are mostly affected by the resonator diameter, parameter that was not considered in this initial study, while it was confirmed that the gap width and the ring thickness have negligible effect on the resonant frequencies (H.K. Cho, 2012).

From the prior results, it can be concluded that an O-Ring resonator, with the original geometry of Figure 3 and parameters of Table 1, reaches the resonance at 1.5603 µm. The resonance is highly influenced by the material and weakly influenced by geometrical aspects.

1.4 Monitoring the PH of the Rain with FBG Sensor

Monitoring the pH of the rain can help to forecast the possible predictable damages for the different materials in order to preserve the original status of the artworks. Fiber Braggs grating sensors coated with pH-sensitive hydrogel have been studied, providing a linear response in the pH range of 5 to 7 with a sensitivity in the simulation of 0.164 nm/pH unit (I. Yulianti, 2010; I. Yulianti, 2014). Optical pH sensors have advantages compared to the conventional pH sensors being free from electromagnetic interference,

wide bandwidth, feasibility of miniaturization, real-time measurement, and possibility of remote sensing (V.N.K. Pabbisetti, 2015; M.F. Jaafar, 2013; L.Y. Shao, 2013).

The outstanding innovation of this sensor is to monitor the pH of the rain for the artworks point by point in real time with a high sensitivity. The actual pH of the water, resulting from the mixing of calcium carbonate and calcium-based compounds, coming from limestone and marble, with acid rain can be measured. This technique allows monitoring small and critical areas like an elbow or an inner thigh of a statue.

The pH sensor suffers from some limitations due to temperature and bending cross-sensitivities (F. Farahi, 1990; I. Yulianti, 2013; T.P. Jones, 1988; M.J.P. Leiner, 1993) that are assumed to be constant and negligible, respectively. This assumption does not seem to be too problematic, as there is a wide variety of compensation techniques for such variables. The accuracy of the sensor is also affected by the multiple resonance peaks and the vast transmission resonance (I. Yulianti, 2013). One of the main advantages of the fiber Bragg grating coated with hydrogel is that the sensed information is encoded directly into wavelength, providing an outcome independent of the intensity of the input light and the loss along the optical system (I. Yulianti, 2013).

The device can be split into two sensors, one using a pH-sensitive polymer with an acidic group and the other with a polymer with a basic group. In contact with certain pH values, the polymers acquire a charge, become ionized and cause a modification of the length of the fiber Bragg grating. The configuration of the device could be composed of two fiber Bragg grating sensors to detect the variations both acidic and basic variations.

A further strength of this device is the dimension. The developed sensor has a length of 10 mm. The small size allows the sensor to be located on almost unreachable artwork elements for pH monitoring.

1.5 FBG pH Sensor

The FBG acts as a wavelength selective mirror being a resonant structure; it is a narrow band filter. If light from a broadband source is injected in the optical fiber, only light within a very narrow spectral width centered at the Bragg wavelength will be back-reflected by the grating. The light that was left will continue through the optical fiber to the next Bragg grating without experiencing any loss. The system of the FBG is a very low-cost mechanism for monitoring of strain and/or temperature within many application fields. In this study, the FBG was modeled to monitor the pH of the rain with the purpose of preserving the original status of artworks. The pH sensor is covered with a hydrogel layer in order to sense variation of pH and thus change the strain of the fiber.

1.5.1 FBG Theory

A fiber Bragg grating consists of a periodic modulation of the refractive index in the core of a single-mode optical fiber. The optical fiber sensor is composed of layers of alternating materials with different refractive indices as shown in the schematic in Figure 14. Each layer boundary causes a partial reflection of the incident optical wave. The pH responsive polymers respond to the changes in the pH of the surrounding water by having a volumetric variation. The expansion of the polymer coating causes a strain on the fiber, modifying the Bragg grating period, that results in a shift in resonant Bragg wavelength, and thus in the sensor response. Peak reflectance is achieved with a design wavelength λ_0 when the configuration of Bragg grating provides constructive interference between reflections.

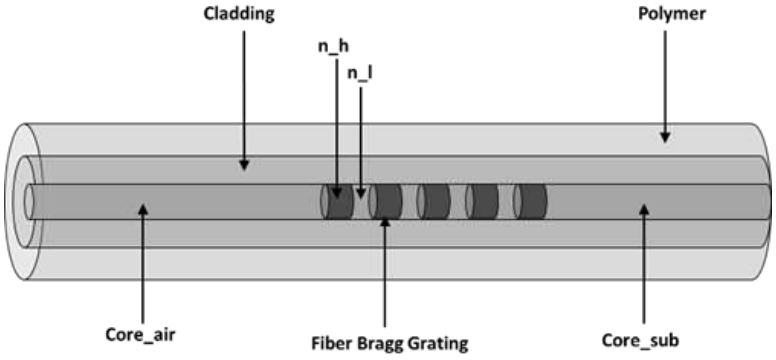

Figure 14. Schematic drawing of polymer-coated fiber Bragg grating pH sensor. Drawing is not to scale.

When broadband source launches light from one side of the fiber, only a specific wavelength, which satisfies Bragg condition, will be reflected while the rest is transmitted without any loss. The wavelength for which the incident light is reflected with maximum efficiency is called the Bragg wavelength (M.M. Werneck, 2013). In optical fiber gratings, the phase matching condition is given by

$$\beta_1 - \beta_2 = \Delta\beta = \frac{2\pi}{\Lambda} \qquad (1.12)$$

where β_1 and β_2 are the propagation constants of the modes being coupled and Λ is the grating period. In the case of FBGs, the propagating core mode that is moving forward couples to the reverse propagating core mode (M.M. Werneck, 2013). Propagation constants remain the same but with a negative sign,

$$\beta_2 = -\beta_1 = \beta \tag{1.13}$$

and thus the (1.12) become

$$\beta - (-\beta) = \frac{2\pi}{\Lambda} \tag{1.14}$$

$$2\beta = \Delta\beta = \frac{2\pi}{\Lambda} \tag{1.15}$$

where $\beta = \frac{2\pi}{\lambda} n_{eff}$. The equation (1.15) becomes

$$2\left(\frac{2\pi}{\lambda} n_{eff}\right) = \frac{2\pi}{\Lambda} \tag{1.16}$$

Ultimately the Bragg wavelength can be written as:

$$\lambda_0 = 2\, n_{eff}\, \Lambda \tag{1.17}$$

where n_{eff} is the effective refractive index of the fiber core.

Changes in the effective refractive index or in the grating period will cause a shift in the reflected Bragg wavelength. The wavelengths, other than the Bragg one, will experience weak reflection at each of the grating planes because of the phase mismatch over the length of the grating. The grating spacing can be changed, during manufacturing, to create Bragg gratings of different center wavelengths. In some papers, the coupled-mode theory (M.M. Werneck, 2013) is used as a technique for the detailed theoretical analysis of FBGs, because it is simple and accurate in simulating the optical behavior and in modeling the optical property of most the fiber gratings.

The simplest uniform fiber Bragg grating structure in optical fiber is an axial (x) and periodic change of the refractive index of the core with a refractive index profile given by

$$n_{eff}(x) = n_0 + \Delta n \cos\left(\frac{2\pi x}{\Lambda}\right) \tag{1.18}$$

where Δn is the amplitude of the induced refractive index perturbation, n_0 is the average index of the fiber core, x is the distance along the fiber's longitudinal axis and Λ is the grating period. The typical value of Δn varies in the range 10^{-5} to 10^{-2} (M.M. Werneck, 2013).

The reflectivity of a grating with constant modulation amplitude and period can be expressed using the coupled mode theory of Lam and Garside as

$$R(l,\lambda) = \frac{\Omega^2 \, sinh^2(sl)}{\Delta k^2 \, sinh^2(sl) + s^2 \, cosh^2(sl)} \tag{1.19}$$

where $\mathrm{R}(\mathrm{l},\lambda)$ is a fraction between 0 and 1 of the propagating optical power reflected by a grating of length l at a given wavelength λ. $\Delta\mathrm{k} = \mathrm{k} - {}^{\pi}/_{\lambda}$ is the detuning wave vector, $\mathrm{k} = {}^{2\pi n_0}/_{\lambda}$ is the propagation constant and $s = \sqrt{\Omega^2 - \Delta k^2}$.

The full-width at half-maximum (FWHM) bandwidth of a grating is the difference between two wavelengths on either side of Bragg wavelength where reflectivity drops to half of its maximum. An increase in length of grating results in reduced FWHM bandwidth. A general expression for the approximate full width at half-maximum bandwidth of a grating is given by:

$$\Delta\lambda_{FWHM} = \lambda_B \alpha \sqrt{\left(\frac{1}{2}\frac{\Delta n}{n}\right)^2 + \left(\frac{1}{N}\right)^2} \tag{1.20}$$

where *N* is the number of grating planes present in grating structure, $\alpha \approx 1$ for strong gratings (for grating with near 100% reflection) and $\alpha \approx 0.5$ for weaker gratings (M.M. Werneck, 2013).

1.5.2 FBG pH Sensor – Material and Method

As said above, the sensor is modeled and its functioning is simulated through Comsol Multiphysics (Wave Optics Module), based on the FEM (Finite Element Method) solver.

The model is studied with 5, 11 and 21 layers of the distributed Bragg grating, showing the different response of the sensor. The fiber Bragg grating is made of two different dielectric materials chosen in this study with nh=2.32 and nl=1.38 as refractive indexes, while air and substrate form the core of the sensor outside the FBG with a refractive index of 1 and 1.5 (Figure 14), respectively. The cladding has a refractive index equal to 1.444. The Bragg wavelength is set to 550 nm, because it is the average wavelength of the visible spectrum and because it minimizes the loss of the light in the fiber. Achieving the Bragg condition requires a layer thicknesses of:

$$t_i = {}^{\lambda_0}/_{4n_i} \tag{1.21}$$

where: n_i is the refractive index of the i-th layer. This model is very innovative because the core consists of four different materials.

The FBG is produced, inducing a periodic or aperiodic variation of refractive index in the core, using an ultraviolet source, such as a UV laser (X. Chen, 2010). The amount of change depends on the time and intensity of the exposure to UV light (X. Chen, 2010). Normally, a germanium-doped silica fiber is used in the manufacture of fiber Bragg gratings (X. Chen, 2010). The polymer is assumed to coat the sensor for the length of 10 mm. The change in pH determines a mechanical expansion of the hydrogel that stretches the dimension of the alternating material layers inside the fiber (H. Li, 2009; H. Li, 2004). The change of the layers' thicknesses creates a shift in the Bragg wavelength. The pH range between 4 and 7.1 is considered to show the performance of the sensor. The percentage reflectance and the wavelength shift are analyzed to provide an estimate of efficiency and sensitivity in the measuring range.

In the study, both a 2-D and a 3-D geometries were analyzed. The planar technology has been chosen to adapt the FBG to the examined surfaces for the synthesis of the device. The cladding material and the Bragg grating will be deposited by using the standard microelectronic processes on two different polymer substrates, making two identical samples. Finally, the two surfaces will be bonded achieving the final structure. External hydrogel is made up of a combination of a solid crosslinked polymeric chain and an adjacent aqueous solution (I. Yulianti, 2013). The pH-sensitive hydrogel will coat the FBG to obtain the final sensor.

Data acquisition will be performed with an optical source, an optical coupler to prevent the reflected light to be propagated back, and an optical spectrum analyzer for detecting the sensor response.

The FBG pH sensor has also been studied with other electromagnetic parameters to allow an easier manufacturability. The fiber Bragg grating is comprised of different dielectric materials compared to the materials for the first sensor of the study; the grating is studied in three configurations with n_h=1.4 and n_l=1.38, n_h =2.2 and n_l =1.38, and finally n_h =3 and n_l =1.38. The core of the sensor outside the FBG is assumed to have a refractive index of 1.451 (X.F. Huang, 2008), which is characteristic of glassy material for the optic frequencies, while the cladding that surrounds the core of the sensor is set to 1.444 (X.F. Huang, 2008). In this scenario, the core is made out of three different materials that are realized with a constant UV light through different exposure times. The choice to set the materials of the sensor to be around 1.5 as refractive index is due to manufacturing considerations. Knowing that this last value is typical of the glass, the standard microelectronic processes on two different polymer substrates will be more straightforward to be used. The sensor has a length of 100 μm. The core of the sensor was set to 6.08 μm as diameter, while the cladding was set to 125 μm (X.F. Huang, 2008).

The Bragg wavelength is considered to be 1550 nm for this second phase, because at this wavelength the loss of any optical fiber is minimum.

1.5.3 Results

In order to validate the measurement system, we have conducted simulations with Comsol Multiphysics (Wave Optics Module), based on the FEM solver. A homemade code in Matlab environment was used for the post processing of the data. The grating period Λ is around 158.9 nm and the Bragg wavelength is around 550 nm.

In Figure 15, the simulation results show an evident shift of the wavelength as a function of pH variation in a time period of 0.05 ns. The chart is based on the assumption of having the original length of the sensor for a pH value equal to 4.

It is observed that the shift in the wavelength presents a growing behaviour, approximately linear, when the pH increases from 4 up to 7.1.

As expected, the wavelength shift, showed in Figure 15, is identical for the three scenarios with a number of layers of 5, 11 and 21 for FBG. The shift in the peak of the wavelength is independent from the number of layers in the model.

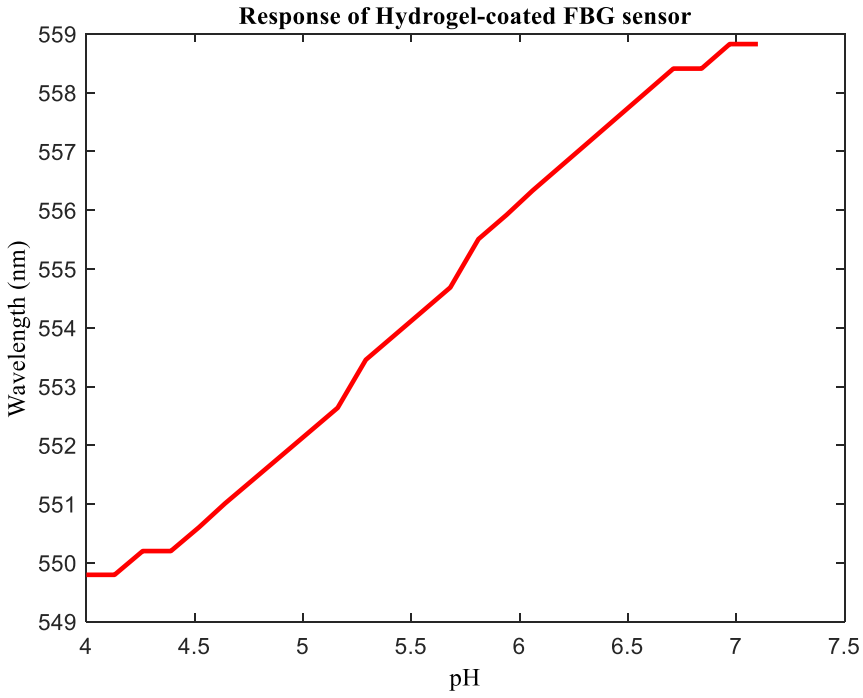

Figure 15. Response of a fiber Bragg grating coated with Hydrogel as a function of pH.

Figure 16 depicts the peak of the percentage reflection in the pH range 4–7.1. Increasing the number of layers from 5 to 21 results in an increase of the reflectance of the initial light intensity, while maintaining the same pattern. As shown in Figure 16, the reflectance peak of the sensor, when 21 layers are considered, is higher than 99.99 %, reaching almost the total reflection.

As depicted in Figure 16 the higher the number of layers in the sensor, the narrower is the range of the reflectance where the peak values will fall.

Figure 17 illustrates that the response of the distributed Bragg grating in the pH range 4-7.1 shows a narrower reflectance range with a higher number of layers in the FBG for vacuum wavelength. The blue lines in the three charts represent the reflectance for a pH of 4, while the red lines represent the reflectance for a pH of 7.1. All the curves for the pH within 4 and 7.1 are not represented for clarity of the chart, but they are in between the blue and red lines.

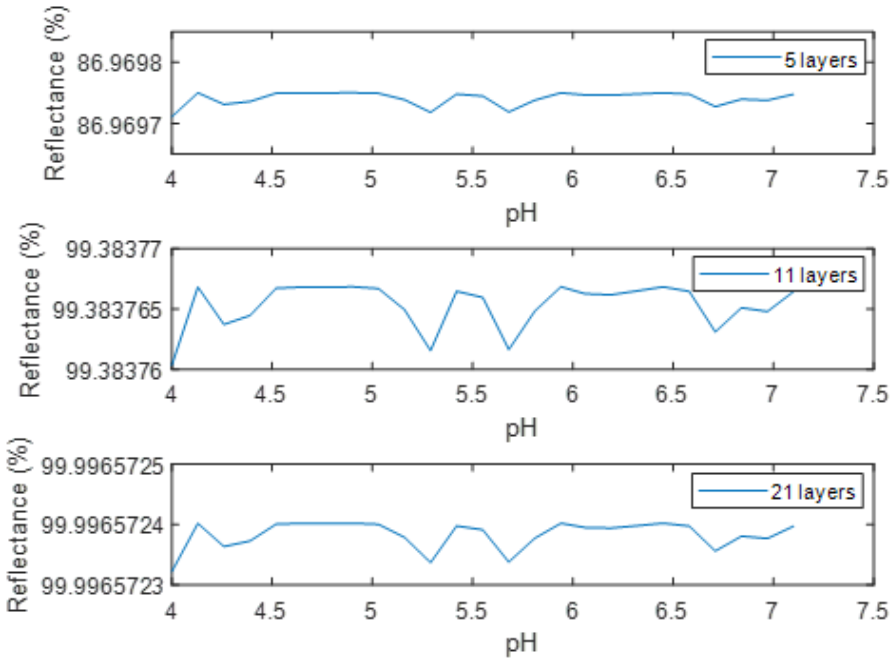

Figure 16. Trend of the peak of percentage reflectance of the distributed Bragg grating in the range of pH 4–7.1 for number of layers 5, 11 and 21.

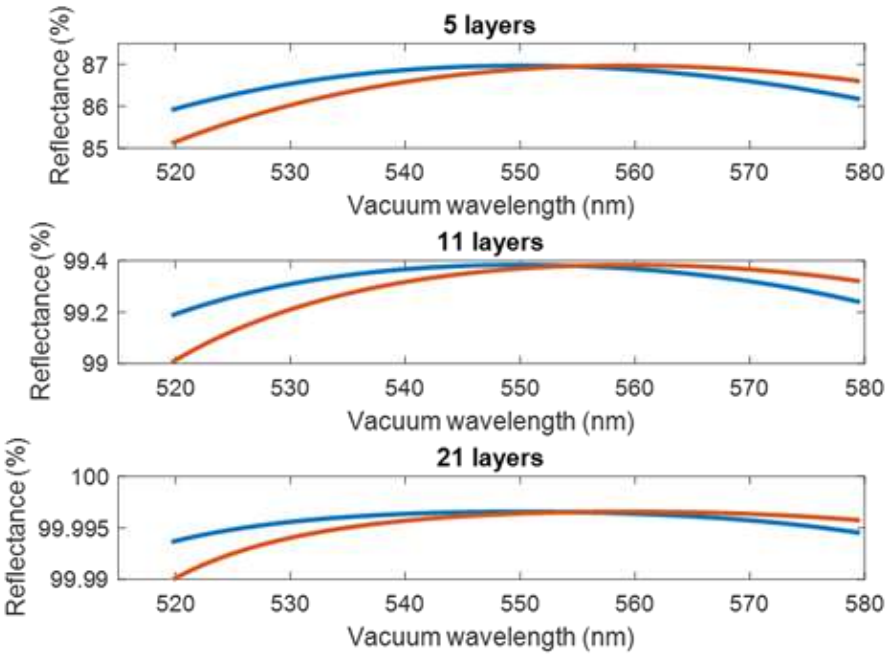

Figure 17. Response of the distributed Bragg grating for all the strains of the hydrogel in the pH range 4–7.1 for the number of layers 5, 11 and 21. For clarity, the curves for pH 4 and 7.1, blue and red respectively, are represented; all other curves are in between the two lines.

Figure 18 shows the percentage reflectance of the sensor for the three different layers of grating. For 21 layers, the reflectance is approximately 100 as illustrated in Figure 18; the higher the number of layers in the sensor, the closer is the reflectance to 100 %.

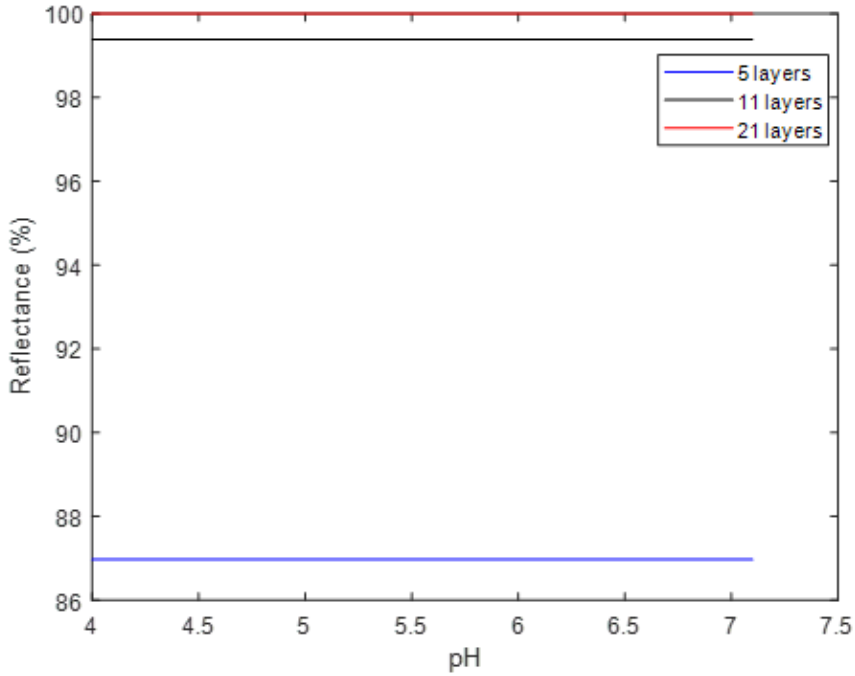

Figure 18. Percentage reflectance of the distributed Bragg grating in the pH range of 4–7.1 for the number of layers 5, 11 and 21.

Concluding, the FBG pH sensor coated with hydrogel has been devised exploiting the hydrogel swelling as a result of the change of surrounding pH in a time interval and its mechanical effect on the FBG.

In this section, the behaviour of the sensor variant, which is made of different materials for the core and the cladding compared to the first one, has been studied. Figure 19 shows the reflectance percentage as a function of the vacuum wavelength in the pH range 4-7.1 for 5, 11 and 21 layers of the distributed Bragg grating each.

In Figure 19 the performances of the sensors with different grating materials are compared to one another, for the number of layers of the grating equal to 5, 11 and 21. The pH values vary from 4 to 7.1. However, only the curves for the extremities of the pH values are represented for clarity of the charts.

In Figure 19 a), b) and c) the grating of the sensor is set to n_h=1.4 and n_l=1.38, n_h=2.2 and n_l=1.38, and n_h=3 and n_l=1.38, respectively. In the scenario a), the reflectance peak is narrower for 21 layers compared to scenarios b) and c), with the highest peak in the three figures always being for the 21 layers. In figure a) the percentage reflectance is very low for the three different configurations of grating with 5, 10 and 21 layers, even if the one with 21 shows a slightly higher peak. It is also evident in the three figures that the reflectance for the 21 layer setup is always higher compared to the 5 and 10 ones. From this analysis, it can be stated that the higher the number of layers in the grating, the higher

the percentage reflectance or peak reflection, as confirmed also with the first sensor studied in the previous section. Moreover, the higher the difference between the refractive indexes of the two materials that constitute the grating, the higher the peak reflection, even if with a wider bandwidth.

Figure 20 shows the reflectance for the fiber with a number of layers in the grating equal to 21, because it is the model that shows the better performance, compared to the others. The reflectance peak for the configuration with the grating equal to n_h=3 and nl=1.38 shows a reflectance power approximately equal to 100%, reaching almost the total reflection in the Bragg bandwidth. The fiber with n_h=1.4 and n_l=1.38 shows a very low reflectance, around 1.15965%.

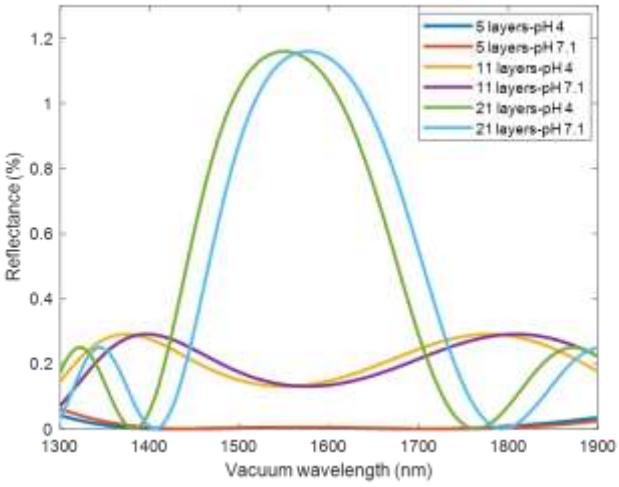

a)

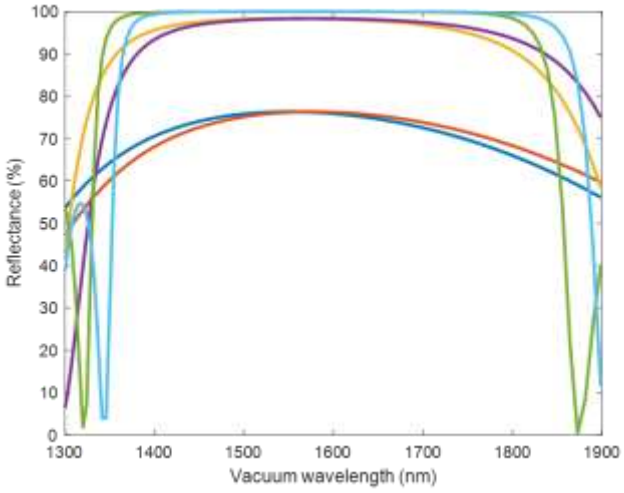

b)

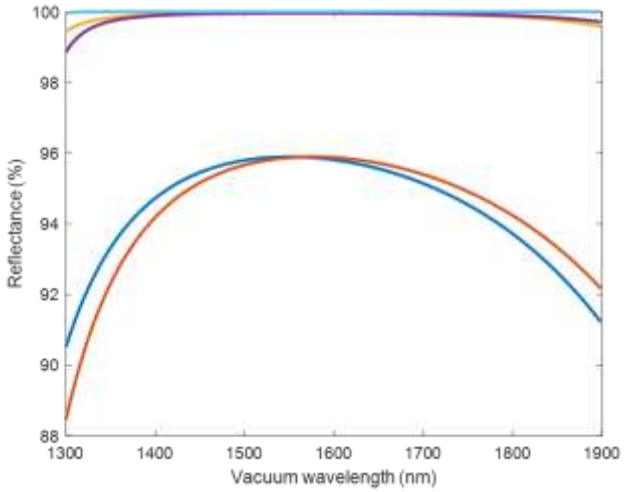

c)

Figure 19. Percentage reflectance of the distributed Bragg grating as a function of vacuum wavelength between 1300-1900 nm in the pH range 4–7.1. The legend is shown only in the top figure for clarity, but it is also applied to the other two figures. a) Grating equal to n_h=1.4 and n_l=1.38 for the number of layers 5, 11 and 21. b) Grating equal to n_h=2.2 and n_l=1.38 for the number of layers 5, 11 and 21. c) Grating equal to n_h=3.0 and n_l=1.38 for the number of layers 5, 11 and 21.

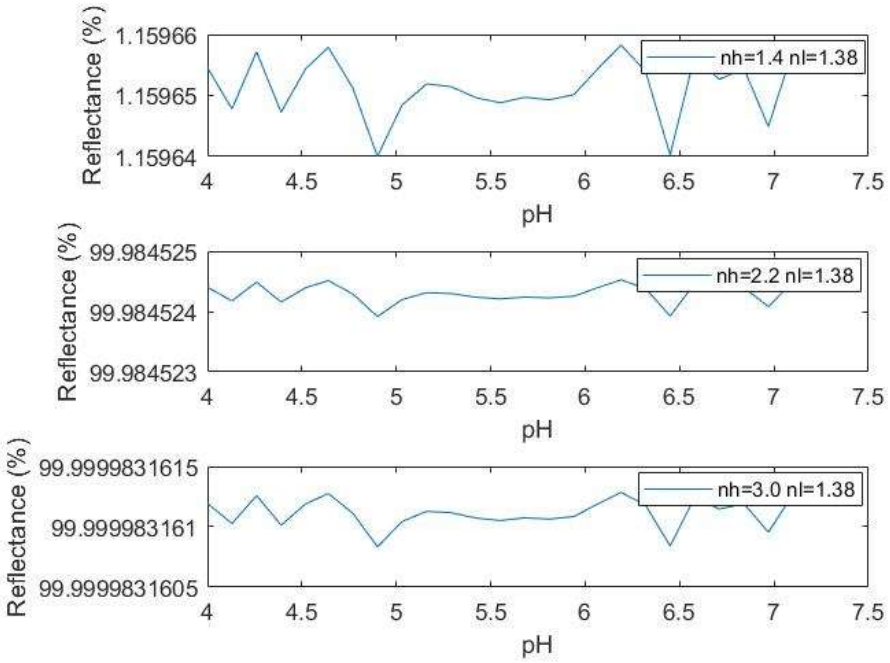

Figure 20. Trend of the peak of percentage reflectance for the distributed Bragg grating in the range of pH 4–7.1 for a grating with 21 layers and refractive index equal to nh=1.4 and nl=1.38, nh=2.2 and nl=1.38, and nh=3 and nl=1.38, respectively.

In Figure 21 the simulation results show an evident shift of the wavelength as a function of pH variation in a time period of 0.05 ns. The chart is based on the assumption of having the original length of the sensor for a pH value equal to 4. It is observed that the shift in the wavelength presents a growing behaviour, approximately linear, when the pH increases from 4 up to 7.1. The sensitivity of the sensors for all different configurations with different materials for the grating provided the same response, because the Bragg grating period is a function of the wavelength and refractive index. This fiber, compared to the one with air and substrate in the core outside the grating, shows a higher sensitivity in the spectrum range under analysis, being around 8.58 nm/pH.

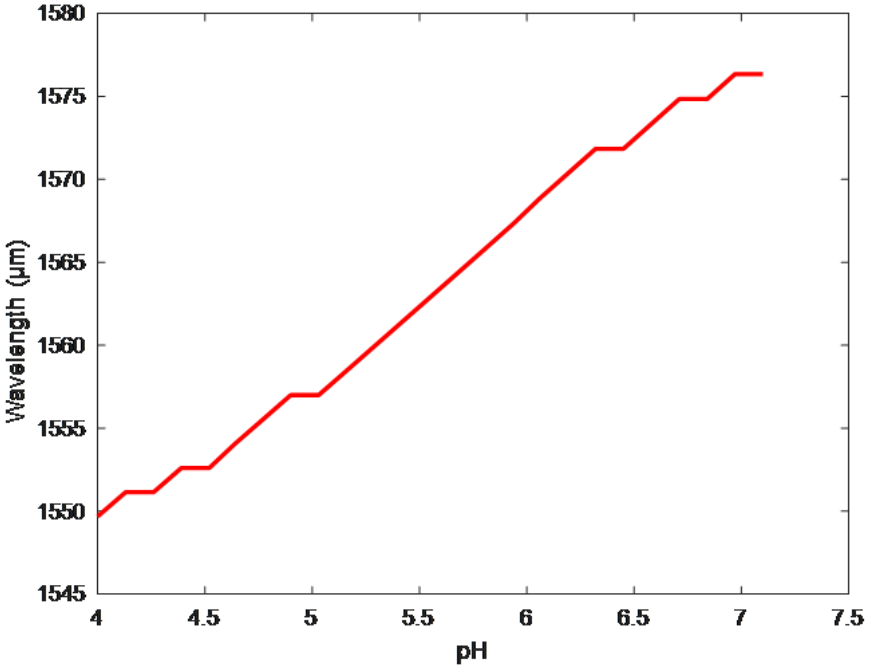

Figure 21. Response of a fiber Bragg grating coated with hydrogel as a function of pH.

1.5.4 Discussion

The response of the sensor in Figure 15 shows approximately linear behaviour in the pH range 4-7.1. Changing the number of layers in the grating does not affect the response of the FBG sensor in terms of wavelength shift, but it has an effect on the reflectance intensity as shown in Figure 16. Subsequently, the sensor was studied with different grating materials for maximizing its performance. In Figure 17, the behaviours of the sensor with different grating materials are compared to one another, n_h was set equal to 1.4, 2.2 and 3 in three sensor configurations while n_l was kept to 1.38. From this analysis it was noticed that the higher the number of layers in the grating, the higher the reflectance percentage or peak reflection, and moreover, the higher the difference between the refractive indices of the two materials that constitute the grating, the higher the peak reflection, even if with a wider stop-band. In conclusion, it can be stated that the optimum sensor has the grating constituted by two materials with n_l =1.38 and n_h equal to a value higher than 1.4 and lower than 3. The purpose is to have the highest sensitivity, thus a high reflectance percentage but also a limited stop-band.

The wavelength drift of the FBG sensor is also induced by bending cross-sensitivity and temperature changes. In this study, these two effects have not been considered. The

temperature and strain parameters will be taken into account for the next generation of FBG pH sensors. These will be compensated with either two further FBG sensors or a single FBG sensor able to measure both temperature and strain, simultaneously. The dedicated system will be placed in series in the measurement chain. As temperature and strain sensors, FBGs have a fast response time due to their small size and volume. Knowing the real-time outputs of the sensors for the temperature and strain changes, it will be possible to accurately measure the variation of pH of the material under analysis, subtracting the effect of these two quantities.

1.6 Conclusion

In this work, an innovative system has been presented to determine the pH value of the rain. The advantage of forecasting the corrosion of monuments is putting optimal restoration programs in place. These are also depending on the materials under analysis and can have an important impact in terms of cost reductions and higher maintenance efficiency.

An additional advantage, due to the small dimensions, is to locate the sensor in modest areas of the artworks without a visual impact. Moreover, the chain of measurement can also be located underground for protecting and preserving the original appearance.

In conclusion, the swelling response of hydrogels to the change of surrounding pH allowed the development of a model of hydrogel coated FBG pH sensor. Modelling the FBG pH sensor for monitoring the rain in archaeology and in cultural heritage provided innovative results in terms of high sensitivity and small dimensions of the device, allowing for better intervention planning, especially when used together with other stone conservations (A. Macchia, 2017). The sensitivity of the first sensor is around 2.91 nm/pH, as confirmed in Figure 15. A second generation of sensors was developed to facilitate the manufacturability. The analysis of the performances of the sensors showed an even higher sensitivity around 8.58 nm/pH. The high variation of the refractive index in the model allowed to discover a sensor with a greatly higher sensitivity and better performances. These innovative results can be applied to all other sensors such as strain gauges and thermometers that use the same physical principle.

Moreover, this sensor, for the future developments, will be integrated with the optical ring resonator in order to improve its performances. Even though the sensor has very small dimensions with a length of 10 mm for the original configuration and 100 µm for its variant, the goal will be to reduce the size even more for medical applications.

2 Chapter 2

Tag Recognition for the Structural Monitoring

2.1 Introduction

Simultaneously to the development of the FBG sensor for monitoring the pH of the rain, an innovative methodology for measuring the cracking in the field of Structural Health Monitoring of cultural heritage to protect and preserve the artworks, is presented. The minimum invasiveness of this methodology allows to preserve the aesthetic appearance, a fundamental requirement in monitoring cultural heritage. The core of the acquisition system is composed of two small adhesive tags to be attached on the artwork surface, and a high-resolution camera acquiring images of the tags. The relative distance between the optical tags is determined using advanced least-squares fitting of quadratic curves and surfaces algorithms for the objective function. Here, the bi-dimensional Gaussian as objective function has been taken into account, in order to find the best configuration for determining the fitting parameters, useful for the SHM. A simulation for tuning fitting algorithm parameters was run. Then the methodology through an experimental session was validated.

The traditional approach used in Structural Health Monitoring (SHM) involves performing static and dynamic tests and measures, both occasionally or periodically, for long periods. Static monitoring techniques aim at detecting the structural characteristics (slow deformation and displacement) of a structure.

The cultural heritage is usually monitored after specific periods of time or after particular events, like earthquake, to evaluate the status of the structures or artworks (V. Gattulli, 2016). Many SHM methods were used, after the terrible event in the town of L'Aquila in Italy, to assess the actual structural integrity and to evaluate the suitability of

the reconstruction phase (V. Gattulli, 2016; C. Gentile, 2016). Typically after a violent earthquake, extensive visual inspections, non-destructive material testing, and ambient vibration tests are performed (A. Saisi, 2016). Dynamic monitoring systems have the purpose to detect and record any variation of the parameters related to the environment or to the structure under control, like cracks opening, deformations or stress (R. Ceravolo, 2017). The most commonly used sensors in SHM are as follows: strain gauge, vibrating wire strain gauge, electrical strain gauge, optical fiber Bragg grating, tape extensometer, borehole extensometer, accelerometer, pressure sensor based on diaphragm type and quartz, temperature sensors based on expansion, thermistors, thermocouple (M.-G. Masciotta, 2016; J. Garcia-Palacios, 2016; L. Dinia, 2017; M. Baskar Rao, 2006). Most of these sensors have drawbacks, for instance, they are susceptible to ambient noise frequency, inaccessibility to remote areas, fragile nature (M. Baskar Rao, 2006). For these reasons as well as pollution related issues, the common natural catastrophic events, and the physiological aging of artworks, researchers are forced to develop and realize more innovative techniques and devices for monitoring the health of the cultural heritage. Other methods have been studied on steel structures for the load monitoring and the bending moments' determination, deflections and deflection profiles of the structures. The Electrical Strain Gauges have been studied and used for this last purpose (M. Baskar Rao, 2006).

A series of accelerometric monitoring systems and displacement transducers were used for this purpose, deployed temporarily or permanently, for continuously monitoring changes on more critical structures (V. Gattulli, 2016). Fiber Bragg grating sensors were used to monitor mechanical and thermal strain on structures, leveraging the different response of the sensor due to deformations and, therefore, changes of the grating period (V. Gattulli, 2016). Piezoelectric accelerometers, widely adopted in this field, compared to the other accelerometers, have the advantage of the piezoelectric material properties, producing current when subjected to a variable force. These sensors proved to be both robust and reliable, as well as stable over time, but they present the fundamental limitation at frequencies below 1 Hz (V. Gattulli, 2016).

More recently, a further measurement technique became prominent, the digital image correlation (DIC) that is used to measure displacements of parts within multiple digital images (N.A. Hoult, 2016). This method was introduced as an alternative to the traditional methods described above.

One of the main advantages of the DIC is the capability to provide full-field surface displacement measurements. As for the tag recognition technique, the DIC provides measurements of crack's movement as long as this happens within the sector of the

digital image (N.A. Hoult, 2016). However, this method presents some limitations on the crack slip measurements.

The development of a technique to measure crack movements by Hoult provided innovative results for evaluating changes in shear crack width in reinforced concrete and slip using DIC. In the experimental test setup Hoult and his team were able to reach an average spatial resolution for the digital images of 0.048 mm/pixel (N.A. Hoult, 2016).

However, these technique do not make possible investigations of structures in a non-invasive way, as they involve placing of elements with a not negligible mass, aggressive anchoring methodologies and a noticeable visual impact. To overcome these drawbacks, the so-called Optical Tags were introduced. The tag recognition method combines different characteristics of many sensors, already widely used and discussed above, with a minimal invasiveness, high accuracy, and very high sensitivity. It can be seen as a system to monitor micro-cracks on the cultural heritage with the goal of minimizing the cost for the timely restoration. The tags are adhesive labels with appropriate images. The absolute and relative position, with the three-dimensional rotations of this image can be determined, using advanced fitting methods and algorithms. This system is inspired by a work published some years ago: to determine the position of the stars from high-definition telescope images (R. Suszynsk, 2015). The determination error of the star tracker was greatly depending on the centroiding algorithm, the method for estimating the centroid of the star. The optics of the stars were slightly defocused in order to spread out the light on several pixels to optimize the detection of the center of the centroid (T. Delabiey, 2014).

In a recent study, cracks on different concrete structures were investigated (H.W. Cho, 2016), by means of image recognition technique. The small cracks identification for the artworks would allow the avoidance of modest fractures growing on the structural cracks (H.W. Cho, 2016). In this scenario, the development of crack image-recognition technique has the potential to reduce human effort and time needed for the reliance on visual inspection by experts. The experimental validation proved that shooting distance and illumination changes are the two most important factors influencing the methodology. The capability to recognize cracks in an acquired image depends, in addition, on the spatial resolution of the camera (H.W. Cho, 2016; F. Mangini, 2017). The aim of this paper is the validation of a novel methodology for detection of micro-displacements between parts of an artwork, through the placement of mini-invasive optical tags and video acquisition. This paper is organized as follows. In Section 2, we introduce the theoretical approach of this new structural monitoring system, in particular, we explain the mathematical models and the considered algorithms.

In Section 3, we present the materials and the adopted methods. Preliminary simulations, followed by real measurements in a controlled environment, were performed through the validation process to reach the expected goal. In Section 4, we present some measurement results to calculate the accuracy of the measurement system and to determine the best fitting algorithm. Finally, in Section 5, some discussions are drawn.

2.2 Tags Features, Theoretical Approach, and Simulated Measurements

The described methodology has been already used in astrology to determine the star centroid from the reconstruction of the point spread function (PSF) analyzing the telescopic images of space portions. The methodology is based on the fitting curve method. The appropriate parameters, to be used for monitoring existing cracks on a cultural asset, are determined with a fitting algorithm of an objective function.

The tags under study are the following: cylindrical or circular, Gaussian tag, Laplacian of the Gauss function and as last the Gumbel tag. The need of studying the different tags profile and the objective to identify the best tag is due to images distortion, blur, etc. because of images acquisition. Below are listed the functions of the tags.

Circular function:

$$f(x,y) = A\left[(x-x_0)^2 + (y-y_0)^2\right] \leq r^2 \qquad (2.1)$$

Gaussian function:

$$f(x,y) = Ae^{-\left[\frac{(x-x_0)^2}{2\sigma_x^2}+\frac{(y-y_0)^2}{2\sigma_y^2}\right]} \qquad (2.2)$$

Laplacian function:

$$f(x,y) = A\left[\frac{(x-x_0)^2}{\sigma_x^2} + \frac{(y-y_0)^2}{\sigma_y^2}\right]e^{-\left[\frac{(x-x_0)^2}{2\sigma_x^2}+\frac{(y-y_0)^2}{2\sigma_y^2}\right]} \qquad (2.3)$$

Gumbel function:

$$f(x,y) = Ae^{-e^{\frac{(x-x_0)}{\sigma_x}} - e^{\frac{(y-y_0)}{\sigma_y}}} \quad (2.4)$$

where σ_x and σ_y are the standard deviations along the *x* and *y*-axis, respectively. The images of the 4 functions are shown in the following Figure 22.

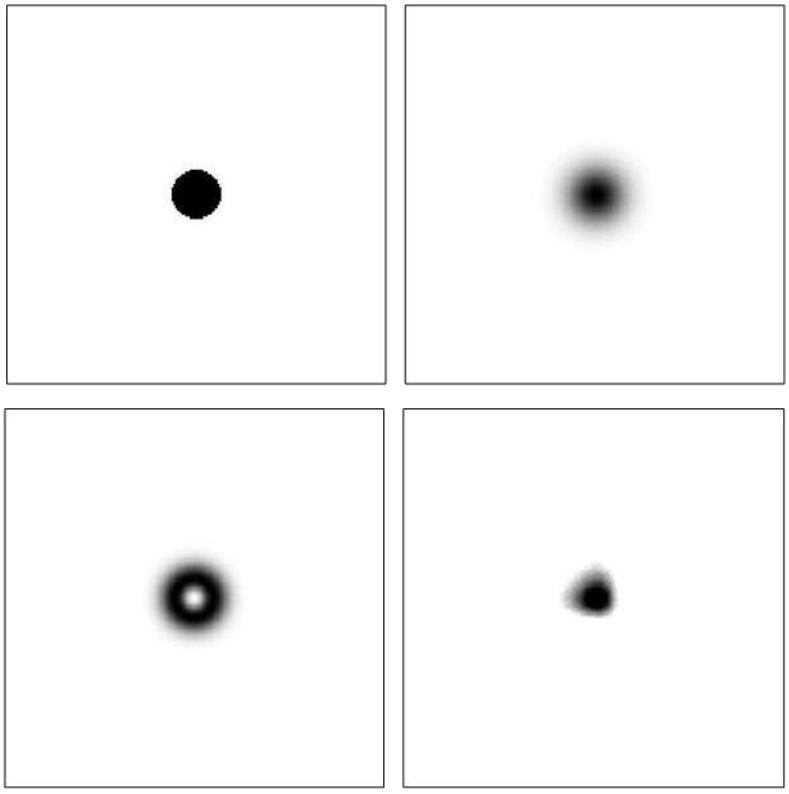

Figure 22. Tags profiles; starting from the top left and proceeding clockwise the followings tags are shown: Circular tag, Gaussian tag, Laplacian tag and Gumbel tag.

The first step to accomplish is the identification of the best objective function to use as a target of the monitoring system.

The best type of tag is determined with translation tests keeping a constant σ; the tags are created with the prior formulas. An ideal tag was used to simulate a real tag, a vertical translation z_0 was added to simulate the tag illumination variation as well as a noise *r* equal to 10% of the maximum value of the function. Below is showed the general formula for a real tag.

$$F(x,y) = f(x,y) + z_0 + r(x,y) \quad (2.5)$$

In particular, to simulate the relative displacement between two tags, the two distributions $\mathrm{f}(\mathrm{x}-\mathrm{x}_1,\mathrm{y}-\mathrm{y}_1)$ and $\mathrm{f}(\mathrm{x}-\mathrm{x}_2,\mathrm{y}-\mathrm{y}_2)$ have been taken into account (see Eqs. (2.7) – (2.8)).

$$F\ (x,y) = f(x-x_1, y-y_1) + f(x-x_2, y-y_2) + z_0\ + r(x,y) \qquad (2.6)$$

Figure 23 represents the function in Eq. (2.6). The method used to determine the displacement, i.e. the coordinates of the center of the function x_0 and y_0 (see Figure 23), is the least-square method of data fitting applied to non-linear curves. In particular, two methodologies were adopted in this context; the first one is the non-linear solving least square method based on the algorithm of the "Trust-Region-Reflective" (J.J. Moré, 1977), while the second is based on the algorithm of Levenberg-Marquardt (J.E. Dennis Jr., 1977; K. Levenberg, 1944; D. Marquardt, 1963). All codes have been implemented in Matlab. By simulating the relative displacement between the two tags through the two functions $\mathrm{f}(\mathrm{x}-\mathrm{x}_1,\mathrm{y}-\mathrm{y}_1)$ and $\mathrm{f}(\mathrm{x}-\mathrm{x}_2,\mathrm{y}-\mathrm{y}_2)$, the position of one of the two tags was determined. This allowed the detection of the best algorithm, in terms of minimization of reconstruction errors and elaboration speed.

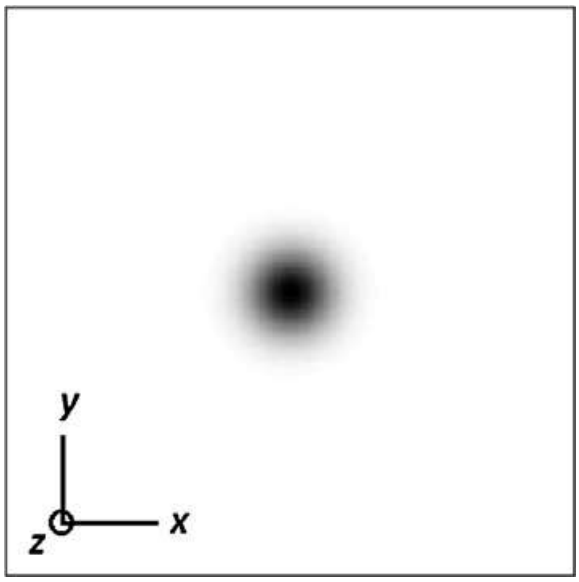

Figure 23. Optical tag profiles: Gaussian tag.

The circular function was the first to be considered, but it presented some limitations due to the blurring of the optical system. The acquisition smooths the images, giving a shape of normal distribution. For this reason, the tag with a Gaussian profile was chosen for the study (see Figure 23). The use of the Gaussian distribution was investigated to

define the performance of the model. In this scenario, the relative distance between the two tags was studied deeply to highlight the advantages.
For the 2D Gaussian distribution:

$$f(x,y) = Ae^{-\left[a(x-x_0)^2 - 2b(x-x_0)(y-y_0) + c(y-y_0)^2\right]} \tag{2.7}$$

where,

$$\begin{aligned} a &= \frac{\cos^2 \vartheta_z}{2\sigma_x^2} + \frac{\sin^2 \vartheta_z}{2\sigma_y^2} \\ b &= \frac{\sin 2\vartheta_z}{4\sigma_x^2} + \frac{\sin 2\vartheta_z}{4\sigma_y^2} \\ c &= \frac{\sin^2 \vartheta_z}{2\sigma_x^2} + \frac{\cos^2 \vartheta_z}{2\sigma_y^2} \end{aligned} \tag{2.8}$$

where σ_x and σ_y are the standard deviations along the *x* and *y*-axis, respectively; θ is the rotation around the normal outgoing from the tag surface. The parameters x_0 and y_0 are important in determining the relative distance between the tags. Nothing prevents from investigating other types of distributions to be silk-screened on the tags. However, the system in its simplest form will be analyzed in this study, to determine its main metrological characteristics. The tag profile used is shown in Figure 24.

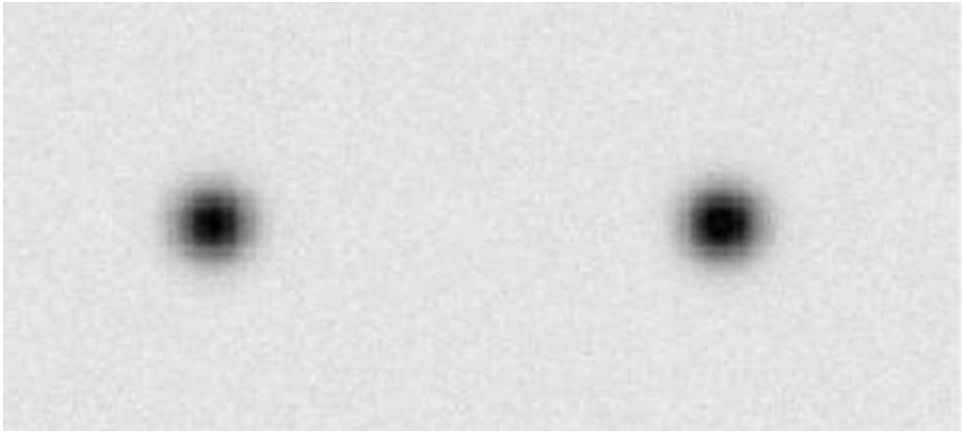

Figure 24. Simulated tags using Eq. (2.6).

2.3 Algorithms Performances

In this section, the two fitting algorithms are compared to one another to evaluate the performances related to the determination of the frames for the Gaussian tags. To improve the measurement process for the algorithms it is considered a ROI around the tag and a fitting of the image through cubic interpolation for both methodologies.

The two algorithms were compared considering images of 200 x 200 px and 400 x 400 px, with $\sigma_x = \sigma_y = 10$, a translation of 20% of the maximum of the function $F(x, y)$ and a random noise (function "rand" in Matlab) of the maximum of the function itself.

The variation of the Tag position has been carried out along the $y = x$ bisector with variation of tenth of a pixel. Figure 25 shows the results obtained with the resolution of 200 x 200 px, while Figure 26 shows the results for 400 x 400 px. In each figure, starting from the top of the left column proceeding counterclockwise the following are displayed: the image of $F(x, y)$, the maximum profile of the function along x and the profile of the Gaussian function from the parameters achieved with the fitting; on the right side of the figures are the relative error between the set center as input and the determined center through the fitting along the *x* axis (i.e. x_0), the relative error along the *y* axis (i.e. y_0), and the last two figures represent the relative error between the standard deviations $\sigma_x = \sigma_y = 20$ and those calculated with the two algorithms. On the horizontal axis of the right graphs, there are the 100 iterations to determine the relative error. After 100 iterations, a displacement of 10 px is reached because each shift is of a tenth of a pixel.

Finally, in Table 2 are presented the averages of the modules of the relative errors for the shift along *x, y,* σ_x *and* σ_y , respectively.

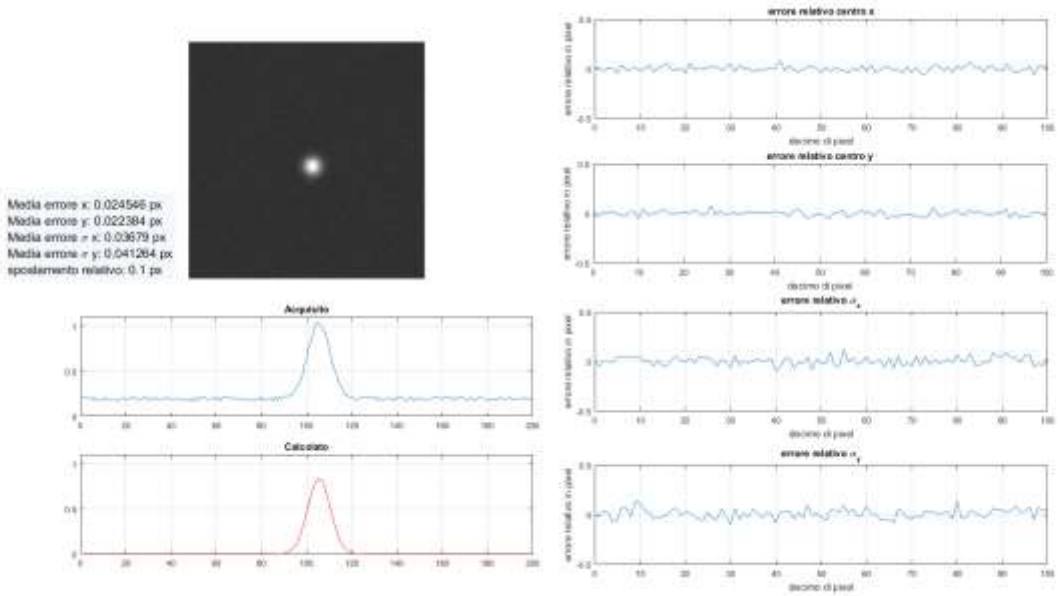

Figure 25: Analysis of the relative errors between the simulated image and the result of the fitting with a Gaussian tag, with algorithm Trust-Region Reflection.

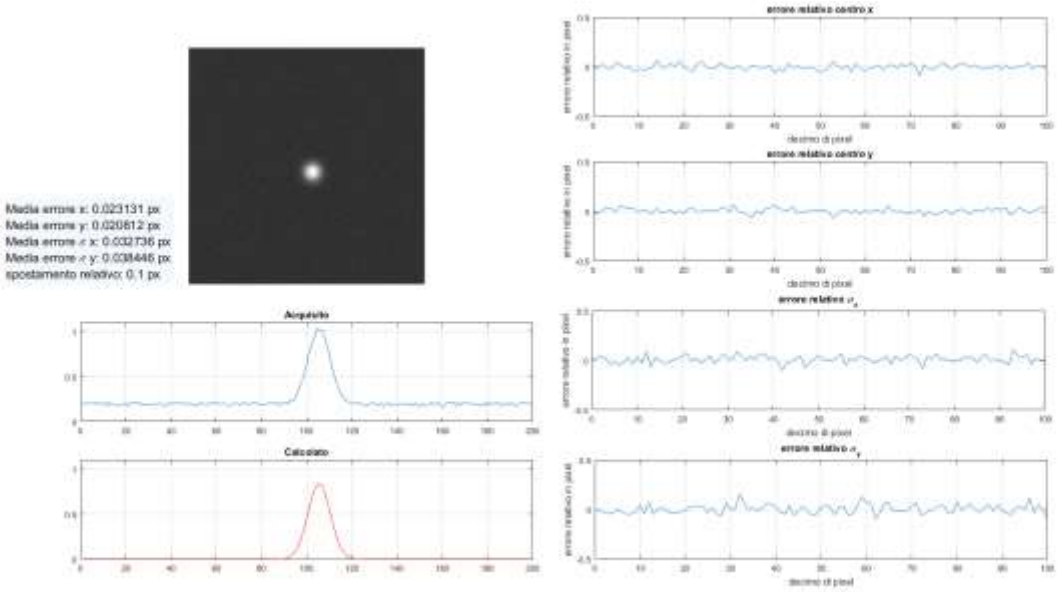

Figure 26: Analysis of the relative errors between the simulated image and the result of the fitting with a Gaussian tag, with algorithm Levenberg-Marquardt.

Table 2: Summary of the results achieved for the Gaussian tag for the two algorithms, a) case with images resolution of 200 x 200 px; b) case with images resolution of 400 x 400 px.

a)	Translation (x,y) with resolution 200 x 200 px	
	Trust-region-reflective method	Levenberg-Marquardt method
	Gaussian	Gaussian
$\lvert x_i\text{-}x_0\rvert$	24,54%	23,13%
$\lvert y_i\text{-}y_0\rvert$	22,23%	20,81%
$\lvert \sigma_{xi}\text{-}\sigma_{x0}\rvert$	36,79%	32,73%
$\lvert \sigma_{yi}\text{-}\sigma_{y0}\rvert$	41,26%	38,44%

b)	Translation (x,y) with resolution 400 x 400 px	
	Trust-region-reflective method	Levenberg-Marquardt method
	Gaussian	Gaussian
$\lvert x_i\text{-}x_0\rvert$	9,91%	11,46%
$\lvert y_i\text{-}y_0\rvert$	11,26%	9,75%
$\lvert \sigma_{xi}\text{-}\sigma_{x0}\rvert$	30,44%	27,71%
$\lvert \sigma_{yi}\text{-}\sigma_{y0}\rvert$	29,15%	30,93%

2.4 Experimental Validation

The setup for the experimental validation was composed of a video capturing system GigE Vision Mako G, a power supply channel with Ethernet cable for data exchange (PoE, Power over Ethernet), and a PC for running the fitting algorithm (but a single-board computer is usable as well). The algorithm used for these measurements was the "Trust-Region-Reflective", as it achieved the best results during the simulation. The core of the test bench was the optic HD camera and the two Gaussian tags, positioned at a certain distance between each other (see Figure 27). The tags and the camera were fastened to an anti-vibration bench. The camera used for the tests was a Mako G-503B (Allied Vision GIGEVision) with a semiconductor sensor. The resolution and the cell size were 2592 px (h) × 1944 px (v) and a cell size of 2.2 µm × 2.2 µm, respectively.

In practical applications, the position and the fixation of the camera to prevent camera displacements are very important. To make the relative distance measurements independent from the position of the camera, it will be enough to use the other fitting parameters, which have not been used until now. In fact, by using the parameters σ_x, σ_y, and θ (see Eqs. (2.7) – (2.8)) it is possible to understand and then correct any movements and rotations of the camera with respect to the tags using a simple and appropriate

rototranslation matrix. The tag was silk-screened on adhesive and opaque paper (see Figure 28), it was decided that the standard deviations of the tag (σ_x and σ_y) were assumed to be around 6.6 mm. In the laboratory, the tags were placed on two micrometer screws-rail guide with a resolution of 10 µm, to simulate a controlled enlargement of a crack.

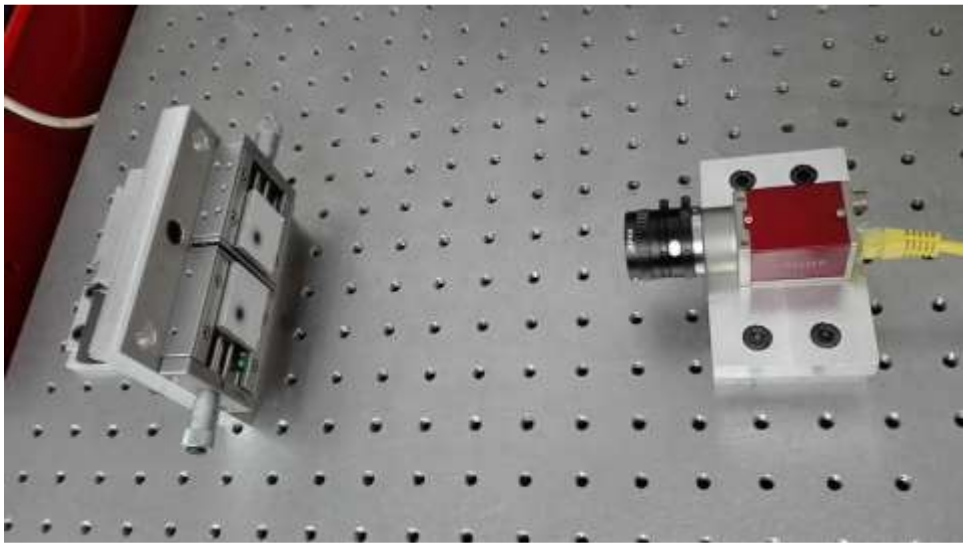

Figure 27. Test bench. The core of the acquisition system is constituted of an optic HD camera and two or more Gaussian tags, positioned at a certain distance between them. The tags and the camera are anchored on an anti-vibration bench. Each support has been made with a certified micrometer accuracy.

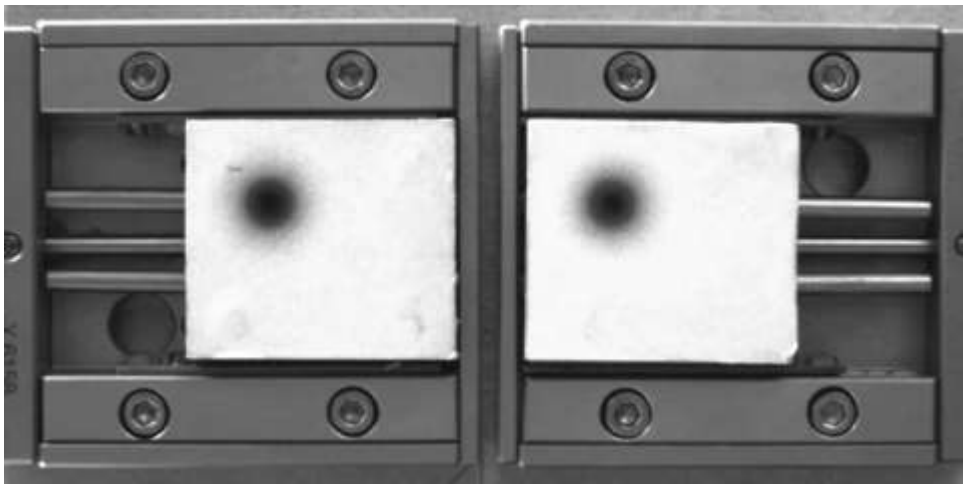

Figure 28. Acquired frame.

2.5 Results

2.5.1 Results – Simulated Measurements

Images with different resolutions: 100 × 100, 200 × 200 and 400 × 400 px, with a vertical translation z_0 equal to the 20% of the maximum value of $f(x, y)$, and with a random noise $r(x, y)$ equal to 10% of the maximum value, were collected (see Eq. (2.6)). A comparison among all the images was performed to identify the best algorithm. The deviation/displacement of the position was applied along the bisector with tenth of pixel variations. The results are shown in Table 3 for 200 × 200 and 400 × 400 px of resolution for the two algorithm cases, respectively.

According to the results in Table 3, the percentage of the absolute error compared to the displacement of 0.1 px improves proportionally to the increase of the image resolution. Although no appreciable differences between the two methodologies were observable to identify the tag position, the “Trust-Region-Reflective” algorithm showed slightly better results. We have taken as a unit of comparison the tenth of pixel because the methodology introduces a kind of oversampling of the image making the tenth of pixel the best comparison unit for our results. Figure 29 shows the initial and final position of the tags in a Region of Interest (ROI) of 400 × 400 px size. The double Gaussian curves represent the acquired image and the reconstructed image with Levenberg- Marquardt fitting algorithm, both passing through the maximum values. The right tag in the figures is kept still. A displacement step of one pixel was considered, with a maximum shift of 10 pixels (see Figure 29).

In Figure 30 the relative error between the effective displacement and the computed displacement with respect to the two directions is illustrated. In particular, the upper plot shows the relative error with respect to the x-direction, while the lower plot shows it with respect to the y-direction.

Table 3. Percentage of the absolute error compared to the displacement of 0.1 px of the fitting parameters in the case of 100 × 100 px, 200 × 200 px, and 400 × 400 px of resolution, using (a) "Trust-Region-Reflective" and (b) Levenberg–Marquardt algorithm.

a)	**Trust-Region-Reflective method**		
	100 x 100px	200 x 200px	400 x 400px
$\lvert x_i - x_0 \rvert$	42.74%	19.30%	9.16%
$\lvert y_i - y_0 \rvert$	48.42%	21.05%	8.32%

b)	**Levenberg–Marquardt method**		
	100 x 100px	200 x 200px	400 x 400px
$\lvert x_i - x_0 \rvert$	45.63%	20.26%	9.41%
$\lvert y_i - y_0 \rvert$	44.68%	22.38%	10.17%

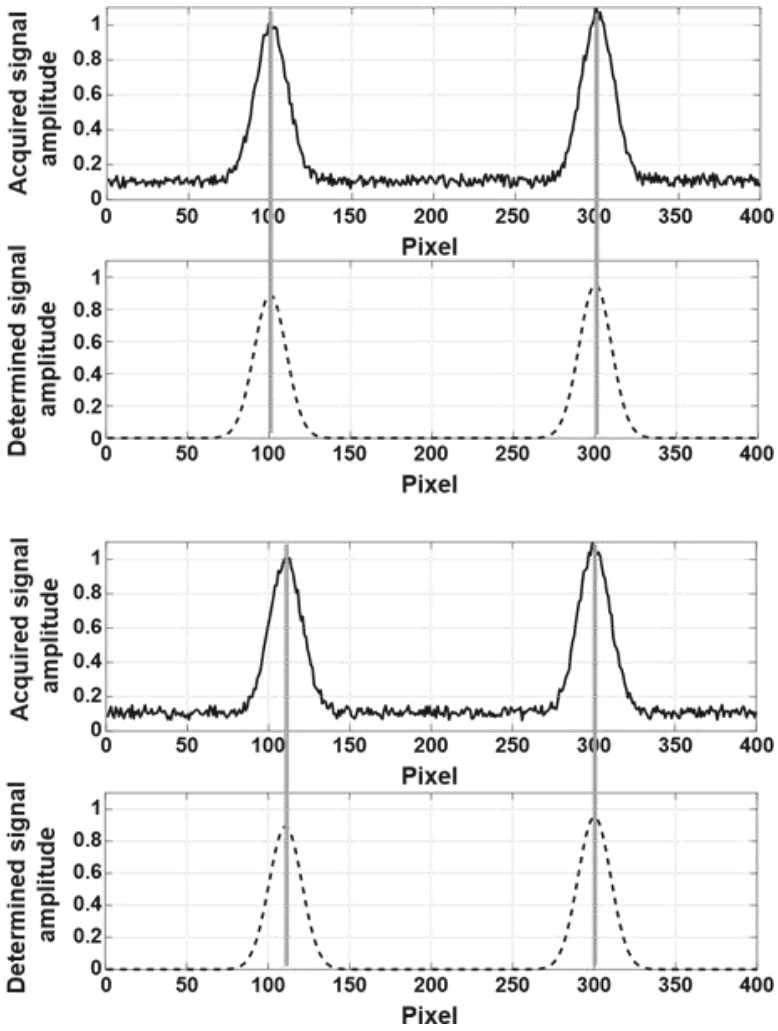

Figure 29. Initial (the first two above) and final tags positions acquired (the second two). The black solid line of each figure represents the signal image acquired along the central row. The gray dashed line of each figure represents the reconstructed image after the Levenberg–Marquardt fitting algorithm along the same row.

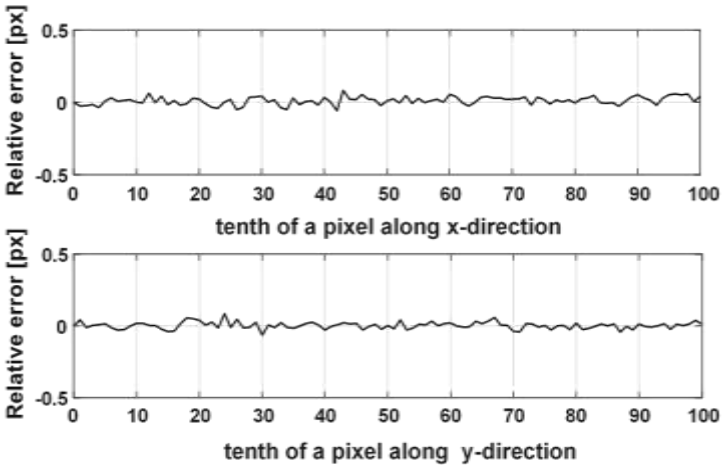

Figure 30. Relative error between the effective displacement and the displacement computed with respect to the two directions (upper: x-direction, lower: y-direction).

2.5.2 Results – Experimental Validation

Tests were performed for the following four camera-tags distances: 25, 50, 75 and 100 cm. For each tag-camera distance, 20 frame acquisitions were considered for each relative position between the two tags. The relative distance between the two tags was varied between 10 µm and 1 cm, and it was considered only the displacement along the x-direction of two Gaussian tags. Figure 31 shows the camera acquisition for a distance camera-tags of 25 cm, representing the measured displacement as a function of the real displacement. For greater readability of the results, the data were organized in three plots, each is characterized by the following measurement range: 10 µm—100 µm, 0.1mm-1mm, and 1mm-10mm. In the Figure, the average of the 20 acquired frames (red-dashed line) and the real relative distance (blue solid line) were represented to show the accuracy of the measurement system. Figure 32 shows the absolute error, the relative error (in percentage), and the standard deviation of the measurements as functions of the real displacement in the case of a distance camera-tags of 25 cm; for each relative distance, 20 frames were averaged. As illustrated in Figure 32.a and b, the relative maximum error is lower than 3%. Figure 32.c, shows approximately a constant standard deviation for all the real displacements with values lower than 4.5 µm.

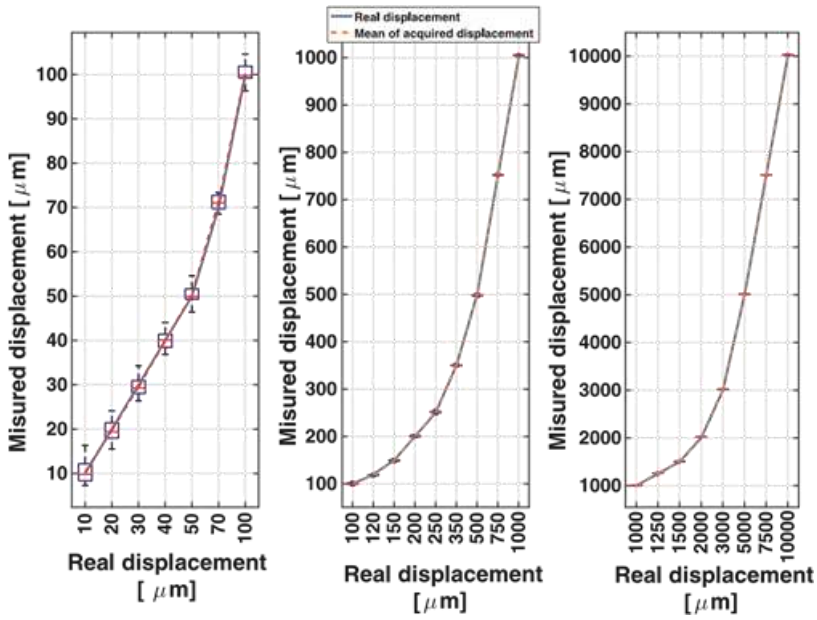

Figure 31. Relative displacement between the optical tags. The camera-tags distance is 25 cm. The relative distance between the two tags has been varied from 10 µm to 1 cm. To make the results more readable, the data have been reported in three plots each characterized by the following measurements range: (a) 10 µm–100 µm, (b) 0.1 mm–1 mm, (c) 1 mm–1 cm. For each figure the average of the 20 acquired frames for each relative distance was reported (red-dashed line) as well as the real relative distance (blue-solid line). Furthermore, for each relative distance the medians are shown (horizontal red line) i.e. the accuracy of the measurement, and the first and the third quartile (the blue box), in order to highlight the standard deviation, then the precision of the measurement system.

Figure 33 shows the measured displacement as a function of the real displacement, in this case for three different camera-tags distances: 50, 75, and 100 cm. These figures highlight the dependence of the method on the distance between the optical acquisition system and the tags. In particular, we can see that as the distance increases, the measurement error increases both in terms of relative error and of standard deviation.

Figure 34.a and b show the relative error and the standard deviation as functions of the real displacement for the different camera-tags distances: 25 cm (solid line), 50 cm (dot-dash line), 75 cm (dot line), and 100 cm (dash line). Both the relative error and the standard deviation increase with the distance. This is due to the fact that as the distance increases, the resolution of the camera decreases, at which point the images acquired have a flattening of the maximum and an increase of the sigma that affect the fitting with an increase of the relative error and of the standard deviation of the measures. This behavior is also highlighted in Figure 35, in which the relative error is plotted in percentage as a function of the camera-tags distance, for analyzing the accuracy of the measurement system. Moreover, for each camera-tags distance the relative error decreases with the real displacement, while the standard deviation remains approximately constant.

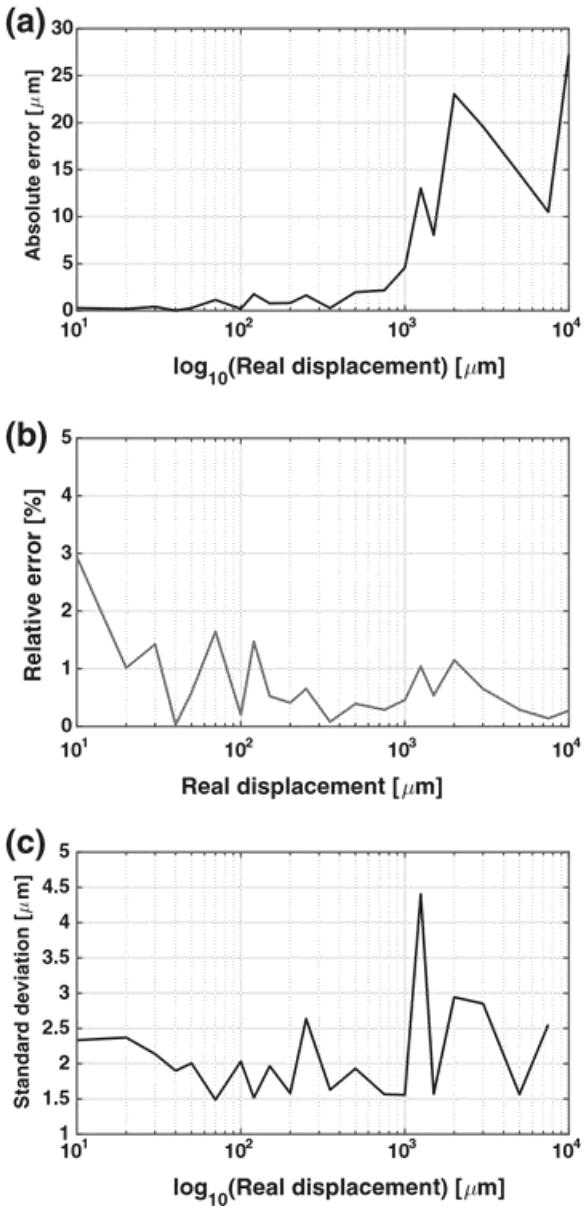

Figure 32. (a) Absolute error, (b) Relative error, and (c) Standard deviation as a function of the tags relative distance, when the camera is placed at 25 cm from targets.

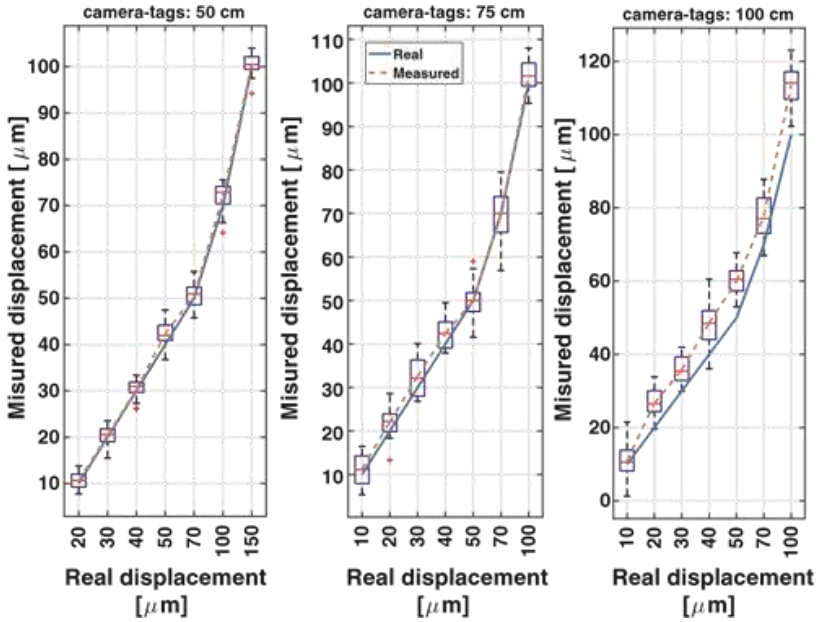

Figure 33. Relative displacements between the optical tags for 3 distance camera-tags: 50, 75, and 100 cm (from left to right). The relative distance between the two tags has been varied from 10 µm to 100 µm. For each figure, the average of the 20 frames acquired for each relative distance was reported (red-dashed line) and the real relative distance (blue-solid line). Furthermore, the medians for each relative distance (horizontal red line) and the first and the third quartile (the blue box) are shown.

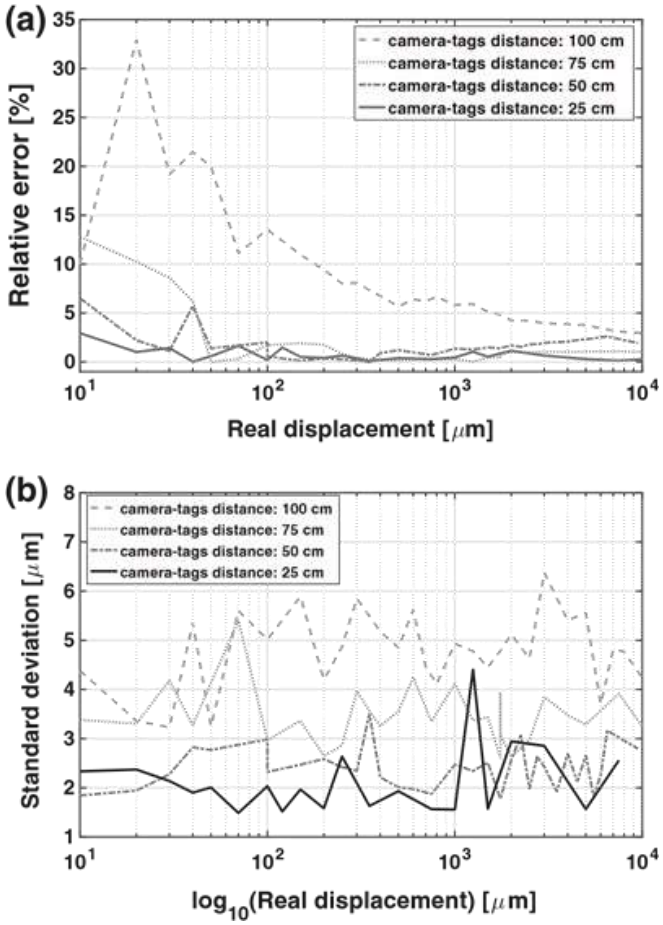

Figure 34. (a) Relative error and (b) Standard deviation as a function of the tags relative distance, when the camera is located at 25 cm (solid line), 50 cm (dot-dash line), 75 cm (dot line), and 100cm (dash line) from the targets.

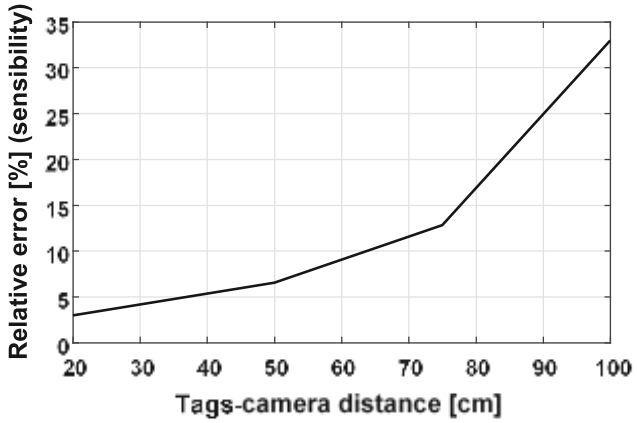

Figure 35. Relative error (accuracy) as a function of the tags-camera distance.

2.6 Discussion

An innovative crack measurement methodology called Tag Recognition has been proposed. In order to develop a measurement system that can also be used for dynamic measurements, such as crack measurements during seismic events, a simulation study was performed. The goal was to determine the best fitting algorithm to maximize the performance of the measurement system. The two most used fitting methods from the literature were compared, i.e. the "Trust-Region-Reflective" and the Levenberg-Marquardt algorithm. At the same time, analysis were carried out on the best fitting reconstruction of the two algorithms. It was found that the best algorithm was the "Trust-Region-Reflective" thanks to the double processing speed, even though the differences, achieved by the simulated measurements, were minimal. It was also found that when the image resolution increases, the relative error and the standard deviation decrease. From the real measurements, in a controlled environment, it was found that with the proposed measurement system it was possible to determine displacements of the order of ten micrometers at a camera-tags distance of 25 cm and with a relative error lower than 3%. The performances of the methodology could be increased by both acting on the distance between the acquisition system and the target, and the choice of the camera's resolution. It was confirmed that this methodology can be satisfactorily used for SHM, in particular, to monitor cracks of Cultural Heritage.

The tag recognition method can also be used for the micro-displacements, for instance, about the displacements due to bradisismic phenomena. It could be effectively integrated with all other established structural monitoring methods, due to different economic and metrological characteristics with respect to all other measurement techniques.

Future works will focus on the study of different statistical distributions to be airbrushed on the tape, and on other fitting algorithms to further increase the metrological performance of the measurement system.

Appendix A - Risk and Perception of Risk in Delivering Anesthesia

A.1 Introduction

Anesthesia is the practice of inhaling specific drugs, volatile anesthetics, to produce the total lack of awareness and pain during surgical procedures (F. P. Branca, 2002). For the long anesthetic-surgical procedures, the modern general anesthesia consists of a mix of both an administration of a drug intravenously and through the respiratory tract with gases and narcotic vapors. Because of the several consequences that the patient could report after the procedures, anesthesia is considered to be high-risk in the healthcare field. But what does risk mean? What is risky? When is the risk acceptable? These are all questions that needed to be clarified over the years and nowadays they are addressed through the risk assessment (P. Slovic, 2002). The general anesthesia is a complex pharmacological and neurological condition characterized by the following:

- suppression of all sensations
- suppression of awareness
- reflectivity control
- fast and complete reversibility
- absence of toxic phenomena on the organism
- ideal scenario for the surgery procedure in the context of operating field

(G. Bellucci, 1990)

When Anesthesia became an independent branch of medicine, experts started to wonder what the risk was during an average procedure for the patient. The meaning of risk has had an evolution over the years; initially, the anesthetic risk was intended exclusively the death as a consequence of delivering anesthesia, beyond any surgical cause (G. Bellucci, 1990). However, the death is not the only risk that the anesthesiologist has to take into consideration. Since anesthesia became a common practice, there have been complications related to eyes, with compressive phenomena and corneal trauma,

and to upper limbs, with paralysis from compression and stretching of the nerves. The use of resuscitation techniques has allowed to recover several patients completely from the operating table, even with neurological deficits often irreversible (G. Bellucci, 1990).

Even if anesthesia is today safer than ever, a culture of safety is spreading in the healthcare system, trying to minimize the risks even further with a continuous improvement approach to reach a higher quality of service/product provided. The quality of service depends on many variables that play fundamental roles in the healthcare system including the technology used, the level of training, personality as well as the perception of risk that can compromise clinical procedures (A.M. Adams, 2001). The anesthetic mortality, and especially the unpredictable one, is notably decreasing over the years thanks to the use of new drugs, the technological advancement, the easiness to obtain a biochemical result, the respiratory control, and the improvement and enhancing of a general monitoring. The anesthetic risk and its importance in preventing adverse related events are linked to a continuous development of anesthesia monitoring and homeostasis of the patient. Tendentially, anesthesiologists are risk adverse and very careful about patient safety because anesthesia can be critical without even having any therapeutic benefits (D.M. Gaba, 2000). The perception of risk may be considered the same as the perception of beauty, temperature or health; there are objective measures but they are inadequate in themselves due to subjective perception (A.M. Adams, 2001). Anesthesia delivery is a branch of medicine in which the risk-benefit assessment is critical. Therefore, the handling and confidence in the use of the technology can have an important impact on the patient safety. Approximately 87% of all incidents that threaten patient safety in the medical environments, where patient monitoring takes place, are caused by human factors, as confirmed by several studies over the years starting from 1950 (A.M. Adams, 2001; T. Walsh, 2002). The results of these studies were not comparable because of constraints in the methodologies and limitation in the scopes, but one important result that emerged was the presence of non-traditional investigations to identify the characteristics of mishaps and to suggest improvements in patient care (D.M. Gaba, 2000).

Manufacturers, in partnership with government agencies, are working toward the continuous development of safer health environments. The needs and expectations of the patients, the confidence of the caregivers, and safe products must meet in order to reach a higher level of patient safety.

A.2 Risk Perception

The survival instinct of all organisms gives the ability to sense and avoid harmful environmental conditions (P. Slovic, 1987). Learning from past experiences is another ability owned by all living organisms (P. Slovic, 1987). Humans have a further capability to reduce risk, which is to change the surrounding environment as well as to respond to it (P. Slovic, 1987). In any humans' activities, there are risks that have to be faced. According to different studies on the perception of risk, the major determiner of the public perception and acceptance of risk is given by feelings of dread (P. Slovic, 2006). For this reason, people are much more concerned about nuclear power than X-Ray radiation from a medical diagnosis (P. Slovic, 2006).

In the current society, the majority of people confide on intuitive risk judgments, called risk perception (P. Slovic, 1987). Risk perception has been studied scientifically in the same way as, for instance, physical and chemical processes (P. Slovic, 2002). The approaches for studying the perception of risk are three: the axiomatic measurement paradigm, the socio-cultural paradigm, and the psychometric paradigm (P. Slovic, 2002). In the current study, the first approach and the third approach will be considered through the examination of the factors that influence the risk perception in delivering anesthesia.

Numerous studies on the risk perception confirmed the initial hypothesis that it can be quantifiable and predictable (P. Slovic, 2002). The judgment of lay people about the risk is related to many different factors as shown in the flowchart in Figure 36 for anesthesia delivery, versus the clear experts' judgement based on the technical estimates of annual fatalities (P. Slovic, 2002). Many models have been created and developed to represent the relationship among perceptions, behaviors and qualitative characteristics of hazards such as voluntary, chronic, common, certainly not fatal, immediate, known to science, not controllable, new (P. Slovic, 2002). These qualitative factors are just a few and each hazard has a unique pattern of qualities. A number of these qualitative risk characteristics make up a hazard's profile and they tend to be correlated with one another, for example, a risk that is voluntary is likely to also be controllable and well-known (P. Slovic, 2002).

Although the dangerous and harmful events are real and objective and the risk can be numerically determined, the subjective perception of the risk plays a fundamental role introducing uncertainties in the outcomes and compromising the resulting behaviors (P. Slovic, 2002). For each person, the risk perception is based on objective factors but also on past experiences, and nowadays it is very much influenced by the news media too (F. P. Branca, 2002). One of the main perceptions that the Americans are facing is that the

risk today is greater than in the past and the phenomenon will continue to increase (F. P. Branca, 2002). Naturally, this perception does not necessarily match the actual scenario that is based on the real negative occurrences, and therefore many factors have to be taken into account when the perception of risk is analyzed. Perception of risk can also have an impact in the society as for how information is reported, and the adverse events about a minor or major accident could be amplified and spread out affecting many other areas (P. Slovic, 2002). An example was given by the seven deaths due to the Tylenol tampering that at the end resulted in more than 125,000 stories in several printing media, causing a damage to the Johnson & Johnson Company of more than a billion dollars due to the damaged image of the product (P. Slovic, 2002).

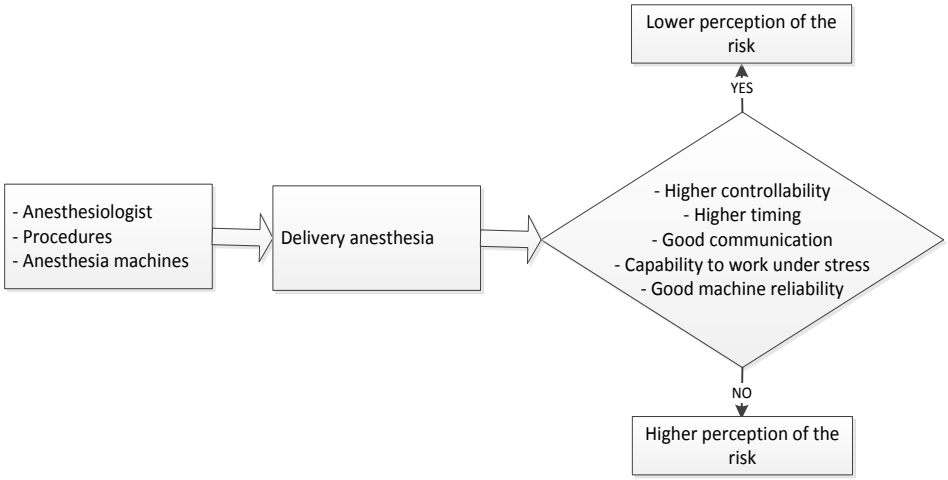

Figure 36. Perception of risk flowchart in delivering anesthesia

According to psychological studies, there are two fundamental ways in which humans process information: the former is a fast, mostly automatic, evolutionarily older system, not very accessible to the conscious awareness and control; while the latter is a system regulated by algorithms and rules, and is much slower and effortful (P. Slovic, 2002). In delivering anesthesia, all these aspects are playing an important role generating variability in the outcome of a specific event. Knowing the weaknesses and the criticalities during the anesthesia procedures, the operators can be educated and trained in order to keep them under control in case of any accidental event, following the system of rationality and conscious awareness.

A.3 Factors Impacting the Perception of Risk

Risks are perceived by people according to the physiological orientation, the characteristic of the risk itself, and other objective factors.

The chance of an unexpected adverse event that cannot be controlled increases the perceived severity of the risk (A.M. Adams, 2001). Human beings prefer to take risks that can be controlled in some way, allowing them to take actions. The perception that a risk is in control gives a sense of safety, downgrading the perceived severity of the risk (A.M. Adams, 2001). Another important aspect is the voluntarism of taking a risk. The perception of that specific risk will be downgraded, as confirmed for example by the difference in attitude towards the risk of contracting an HIV infection from promiscuous sexual behaviors compared to the one from contaminated blood products (A.M. Adams, 2001). The latter magnifies the perception of the risk even if the outcome is the same. An anesthesiologist with high self-control and great knowledge about anesthesia will have a lower perception of risk compared to his colleagues, improving patient safety.

An immediate adverse event gives a higher severity of the risk perception compared to a delayed event (A.M. Adams, 2001). This outcome is logical because during an event that is delayed there is time to take action (A.M. Adams, 2001). Also, a transient or permanent hazard gives a different risk perception with the latter perceived as more threatening (A.M. Adams, 2001). Anesthesia, with its sudden adverse events and its severity, is therefore generally perceived as a very risky medical practice (A.M. Adams, 2001).

The perception of the risk also depends on the personality type of a person. According to David Gaba (D.M. Gaba, 2000), one of the main expert in studying human factors related to anesthesia, the individuals that embark the road to be anesthesiologists typically are a particular type of person who looks for excitements in doing their work (A.M. Adams, 2001). They are just attracted to the higher risk of the world of anesthesia (A.M. Adams, 2001). This aspect can have an influence on how the objective risk is perceived by an anesthesiologist compared to a generic nurse or to external clinical personnel.

The mass media and the spread out of adverse anesthesia related events have contributed to better identify the anesthesia practices and procedures (N. Moerman, 1992; C.F. Swinhoe, 1994). Usually, a patient shows distress and anxiety before anesthesia. The distress is a psychological and physical illness that comes from the awareness of an imminent hazard and it is characterized by widespread fear varying from disquiet until to panic attack. The anxiety can be constitutional of the patient (anxiety-

personality) or it can come from the surgical context (anxiety-status). The anxiety that comes from either the anesthesia or the surgery does not have necessarily a negative impact on the perioperative period, and, in other words, it is a normal psychological predisposition that allows the patient to overcome the procedure to the best. Clinical studies highlighted difficulties to evaluate the degree of anxiety of the patient during the pre-anesthetic consultation because if the anxiety can be expressed, it is often removed by introvert patients (J.P. Haberer, 2001).

Communication is the act to translate the population risk data into clinical risk information that can be easily understood by everyone (A.M. Adams, 2001). There are different categories of communication: verbal, written, and with graphs, charts or maps. In anesthesia, the purpose has always been to share the risk in terms of words or numbers that better convey the right information (A.M. Adams, 2001). Usually, the risk converted into a probability format is not completely understood by the majority of people (A.M. Adams, 2001). The problem of specific probability could be interpreted subjectively by each person without a statistical background. Just thinking about the communication of risk to patients gives the criticality of this aspect. One of the duties of the doctors is to explain the nature, the purpose and all other risk factors of the procedure in non-technical language. Usually, the concept of risk is not clearly defined by the doctors and this results in a lack of providing sufficient information to the patients. The way risk information is presented heavily affects the perception of risk by doctors, nurses, and patients, hereby influencing decision-making (D.J. Malenka, 1993). Giving emphasis on the positive aspects of surgery results will have a persuasive effect on the patients to agree to treatments even if the two statements are objectively equal. Saying that the therapy is 70% effective has a different perception than stating that has 30% of failure rate. This is known as positive framing and has an important impact on the perception of the risk (D.J. Malenka, 1993).

Reliability plays a key role in the caregivers' perception of risk. Expectations concerning the life of an anesthesia machine may vary and may affect how the risk is perceived. Reliability is the ability of a product to perform its intended function over a period of time and under prescribed environmental conditions (D. C. S. Summers, 2006). The main factors that can affect reliability, and thus the perception of risk, are improper design, poor construction materials, faulty manufacturing assembly, inappropriate testing, damage during shipment, improper start-up, physical damages, lack of maintenance, just to name a few (D. C. S. Summers, 2006). This explains why the manufacturer must pay attention to the customer's expectations concerning the product's intended life and environmental condition for use. An anesthesia machine that has several failures over its life increases the perception of risk of the operators in using it, that's why it is very

important to also adopt a preventive maintenance program to increase the effectiveness, lower the risk of failure, and increase components life.

A.4 Critical Relationship Anesthesia Delivery – Patient

One of the main aspects of the evaluation of anesthetic risk is the clinical status of the patient before the surgery. Regarding this aspect, a large portion of anesthesiologists refers to the "American Society of Anesthesiologist" (ASA) classification, which considers the patients divided into 5 classes (Table 4) depending on their "physical status" (P.M. Osswald, 1998).

Table 4. Event result distribution for 2016 and 2017

Class	**Physical Status**
I	A healthy patient
II	A patient with mild systemic disease
III	A patient with severe systemic disease that is a constant threat to life
IV	A patient with incapacitating disease that is a constant threat to life
V	A moribund patient who is not expected to live 24 hours with or without surgery
E	Emergency case

The E class is added to the classes of Table 4 when the operation is carried out in emergency. The ASA classification is not a direct formulation of the anesthetic risk; it is used often thanks to the simplicity and great predictive value. The main weaknesses of the ASA classification are ignoring the age of the patients, the type of surgery and the type of anesthesia. Moreover, some complications in delivery anesthesia are unpredictable, like the anaphylactic reactions, prolonged curarization, and incidents due to human errors or machine failures. Despite the prior considerations, the ASA classification is a useful indicator (J.P. Haberer, 2001). A patient that is classified ASA3 or ASA4 makes the anesthesiologist to be alert and it justifies specific anesthetic techniques and monitoring devices.

In the clinical practice, the use of systematic tests for evaluating the level of anxiety of the patients is not feasible. The empathetic and careful attitude of the anesthetist and the collected information play an essential role in reassurance from eventual expressed and hidden fears.

A.5 Critical Relationship Anesthesia Machine – Operator

The set-up of the anesthesia machine in the operating room can also lead to errors. Figure 37 shows a typical anesthesia machine set-up in a hospital. The configuration of cables, hoses, different surgery tools can be messy and be the reason of human errors. A clean and organized configuration can reduce the operator's perception of risk because it provides the feeling of shorter response time in case of emergency.

An anesthesia machine can be characterized by several failure modes contained into 4 main failure groups:

- Pneumatic leak
- Display assembly failure
- Electronic failure
- Vaporizer and gas module failures.

The failures listed above are the main categories where the majority of deficiencies falls. The impact that these failures have on the perception of risk is very critical both if they are real failures and apparent ones. An aspect that increases the breakdown rate of anesthesia machines is the use of improper cleaning agents (non-recommended by manufactures) or improper cleaning methods; this contributes to giving an impression of unreliable devices, increasing the perception of risk in using anesthesia machines.

Figure 37. Typical anesthesia machine set-up during a case.

A.6 Statistics on the Perception of Risk

Anesthesia is a branch of medicine where adverse events are more frequent than in many other branches. Precise and accurate reporting of adverse events and errors are considered to be necessary for improving patient safety (G.C. Heard, 2012) because “you can’t fix what you don’t know about” (J.P. Bagian, 2001). Despite the expectation that adverse events will be reported, usually attitude, emotional factors, and possible human errors during the procedures may influence the reporting of these events (G.C. Heard, 2012).

In the hospitals, and especially in the operating rooms, where anesthesia machines are used, there are physicians, nurses, anesthesiologist, patients and each one has different ways to describe the same event and to perceive risks (B.D. Winters, 2009).

Various studies were conducted to analyze the tendency of adverse events in anesthesia over the years. In a study during 2012, 4244 anesthesia procedures were

analyzed with 1.25% having complications. This result was compared to the previous year with a percentage of complications of 5.4% (M. Belavic, 2013). A tendency to reduce the number of complications was noted (M. Belavic, 2013). The reduction of adverse events was the result of continuous reporting that led to an increase of awareness on the events and an adoption of preventive and remedial measures (M. Belavic, 2013).

The perception of risk was also analyzed during studies to explore acceptable critical practices in anesthesia. Workplace observations and interviews, directed by Smith (A.F. Smith, 2006), were conducted with anesthesiologists and anesthetic staff. 19 interviews and over 130 hours of observation were recorded (A.F. Smith, 2006). During the course of 50 anesthetic procedures, 103 minor events were observed. None of them was considered by the caregiver important enough to offer the potential to improve safety (A.F. Smith, 2006). The interesting result was that during the departmental meeting at the hospital, the medical staff discussed just 28 of these events and just 5 were considered critical (A.F. Smith, 2006). The conclusion of this study gave the opportunity to focus on how the words “acceptable” and “critical” were perceived and, thus, how the risk was perceived. Unfortunately, this subjective perception affects the formal reporting of the adverse events (A.F. Smith, 2006). During the interviews of the hospital personnel about critical cases, two factors seemed to be very important in affecting the procedures. The first is the controllability, which means to be in control or having the perception of being in control; giving some doctors the license to downgrade some high-risk events. The second is the miscommunication among the different figures working in the operating room about the risk, where each one is having a different perception. According to the result of the study conducted by Smith, anesthesiologists perceive adverse events as “significant moments” in the acquisition of their expertise (A.F. Smith, 2006), fundamental to improve the controllability and timing for the likely future of critical events. At the same time reporting adverse events could lead to criticism and censure from colleagues (A.F. Smith, 2006). For this reason, sometimes they are not reported, considering them as non-critical.

According to further past studies the equipment is involved approximately in between 15%-30% of all the intraoperative problems, and the delivery part for anesthetic and oxygen is the most common responsible for the failures (P. Dalley, 2004). Human error seems to be responsible for around 90% of the failures involving the anesthesia equipment (P. Dalley, 2004). According to another study, the actual equipment failure constitutes just about 15% of the total number of preventable incidents and 82% of the incidents for the total number of the anesthesia procedures involves human errors (J.B. Cooper, 2002). By understanding where these user errors originate, design changes or other remedies can be adopted and patient safety can be improved.

A.7 Characterization of the Risk

Risk has different meanings: it can be intended, for example, as hazard, as probability, as consequence, as potential adversity or threat, and this is another reason that often causes issues in communication (P. Slovic, 2002).

In this study, the risk is the probability of negative occurrences based on the MDR events. In Figure 38, a fish-bone diagram shows the main causes of risk in anesthesia, viewed as causes of adverse events.

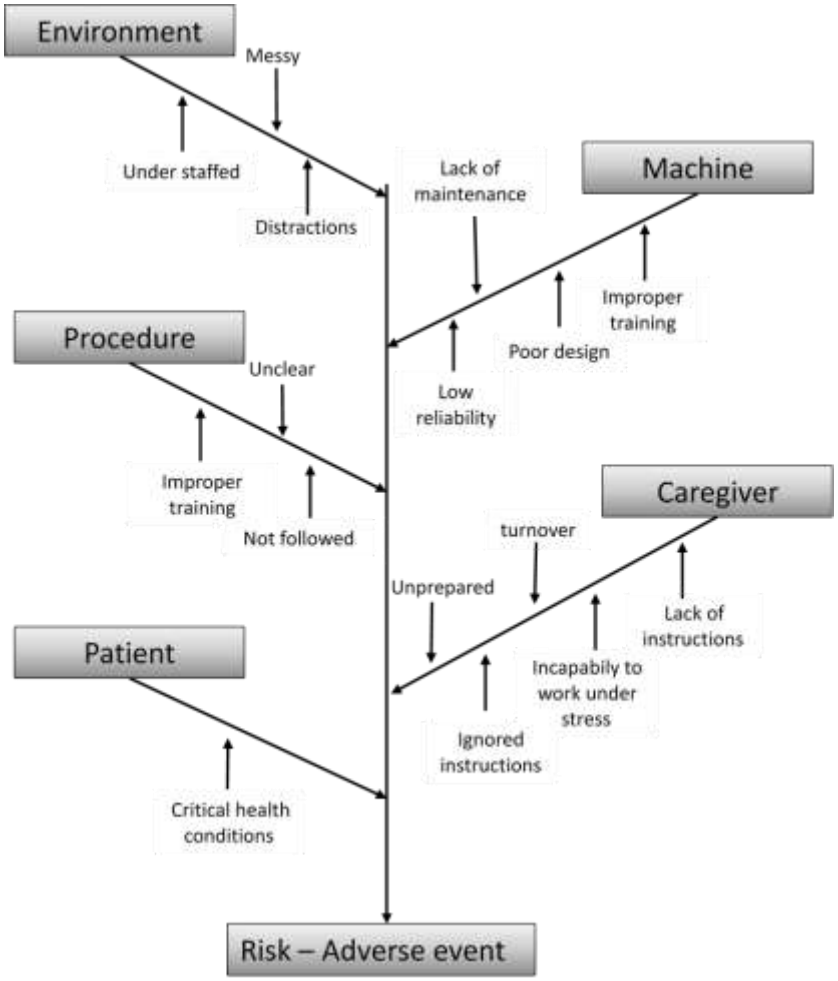

Figure 38. Cause-and-Effect Diagram for Risk-Adverse events.

Typically, in the healthcare system, the tendency is to evaluate the hazards through risk management, which are all the policies and procedures to the task of analyzing, evaluating and controlling the risk, and through risk control, which is a process with the purpose of reducing risks and maintaining risks under specific control. Severity, occurrence, and detectability are three factors used to assign the priority in order to

control specific risks. According to psychologists, people are more afraid of risks that are more severe but with a low probability than they are about the contrary risks (A.M. Adams, 2001). To measure risk in the past, some mathematicians tried to quantify risk introducing expectation value defined as follows:

$$\text{Expectation value} = \text{probability} \times \text{severity} \tag{3.1}$$

The risk is quantified by manufacturers as the product of:

$$R = S \times O \times D \tag{3.2}$$

where R is the measure of risk, S is the severity, O the occurrences and D the detectability. The use of severity and detectability provides an estimate of the risk but, since they are subjective and culturally constructed, they can never actually be measured (A.M. Adams, 2001).

The Medical Device Reportable (MDR) events are used to quantify the actual risk according to the manufacturer.

A.8 Risk as Adverse Events Reported

In the US market, there are more than 50,000 anesthesia machines and this market worldwide was estimated at US$8.1 billion in 2013 and it is projected to reach US$11.8 billion by 2020 (Industry Experts, 2013).

The actual risk is based on the Medical Device Reportable events collected over 2016 and 2017. The analyzed data in this study were collected from MAUDE (Manufacturer and User Facility Device Experience), a database where manufacturers, importers, and device user facilities submit MDR events to FDA (Food and Drug Administration). In Figure 39, the distribution of MDR events reported by the main manufacturers for 2017 is shown. Datex-Ohmeda Inc. / General Electric CO. reported 2135 events, Draeger Medical Systems, Inc. reported 13 events, Shenzhen Mindray Bio-Medical Electronics CO. LTD. reported 10 events, and Maquet Critical Care AB reported 65 events. For these events, the manufacturer “became aware of that reasonably suggested that a device has or may have caused or contributed to a death or serious injury or there was a malfunction that necessitates remedial action to prevent an unreasonable risk of substantial harm to the public health” (U.S. Food & Drug Administration, 2016). “Cause or contribute means that a death or serious injury was or may have been attributed to a medical device, or that a medical device was or may have been a factor in a death or serious injury, including an

event occurring as a result of: failure, malfunction, improper or inadequate design, manufacture, labeling or human error" (U.S. Food & Drug Administration, 2016).

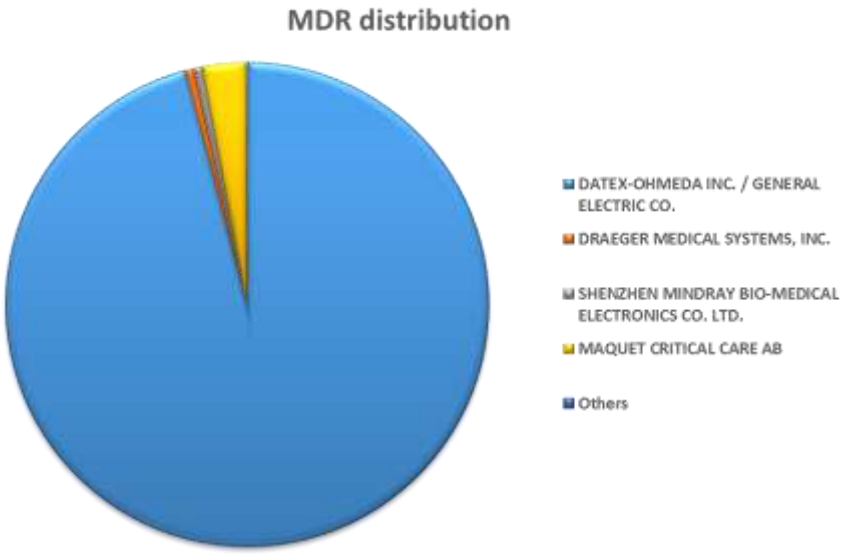

Figure 39. Distribution of Medical Device Reportable events in US market over 2017.

A manufacturer can follow the FDA regulations - 21 Code of Federal Regulations part 803 - with two different approaches. The first is a more conservative one, while the second is a more radical one, reporting almost only cases in which adverse patient events were reported by the caregivers. General Electric CO. reported around 96% of the total MDRs, suggesting that they might have a conservative approach in submitting MDRs and because they might have the biggest portion of the US market (L. Dinia, 2018).

Figure 40 shows the distribution of the event type for the total MDRs reported in 2016. The category Malfunction is 98.93% of the total MDRs, while death is 0.37% and the injury is 0.70%.

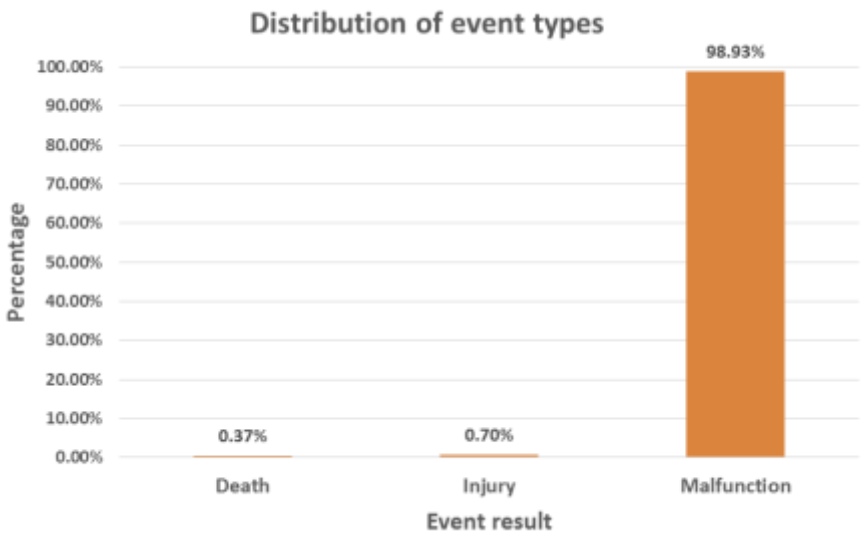

Figure 40. Percentage distribution of event types for the MDR events reported in US over 2016.

In Figure 41 is shown the distribution of the event type for the total MDRs reported in 2017. The category Malfunction, 99.42% of the total MDRs, contains the category Human Error, which provides a measure of the actual risk from the manufacturer perspective.

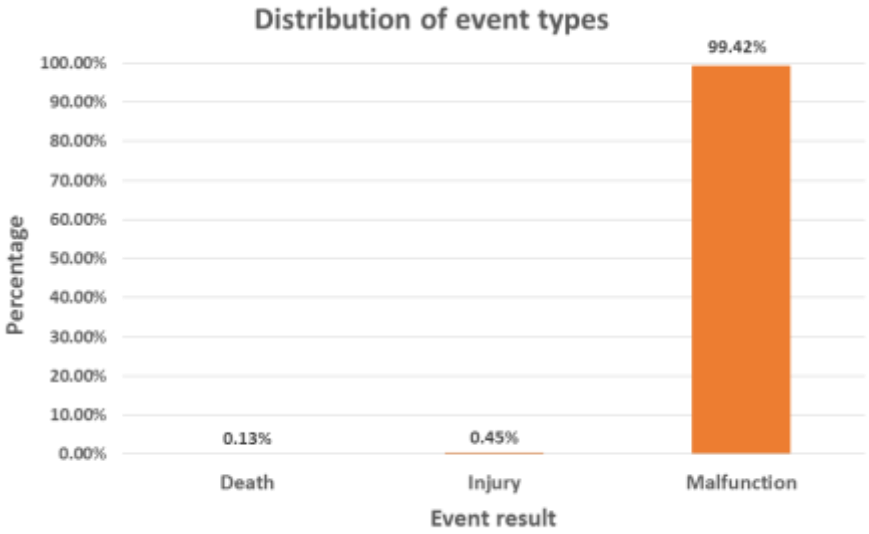

Figure 41. Percentage distribution of event types for the MDR events reported in US over 2017.

The comparison, in Table 5, between 2016 and 2017 shows an improvement in terms of number of deaths and injuries, despite the higher total number of MDRs in 2017 with respect to 2016. The total MDRs reported to FDA in 2016 are 2135, with 8 cases of death and 15 injuries. In 2017 the total MDRs reported are 2226, with a reduction of deaths and

injuries, 3 and 10 respectively. The increase of MDRs in 2017 is the result of the market growth for anesthesia machines. The decrease of deaths and serious injuries is due to better training of the hospital personnel year by year and a higher devices reliability.

Table 5. Event result distribution for 2016 and 2017.

	Event Result			
	Death	***Injury***	***Malfunction***	***Tot***
2016	8	15	2112	2135
2017	3	10	2213	2226

Figure 42 shows the distribution of MDRs reported in US over 2017. There is an increasing trend, shown by the dotted linear regression, over the year and slightly higher distribution during the summer and the last two months of the year.

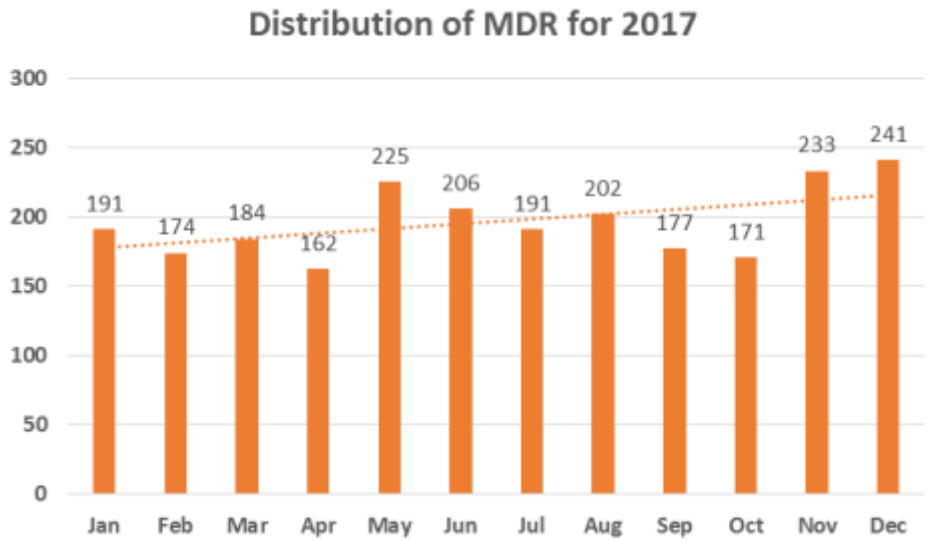

Figure 42. Distribution of MDR events reported in US over 2017.

The comparison between the MDRs reported in 2016 and 2017 (Figure 43) highlights an increasing trend each month from 2016 to 2017. As stated above, this trend is the result of an abnormal growth of the anesthesia machine market with new hospital personnel needed of training about even more complex software and hardware. This trend suggests a tendency of an increasing number of MDRs reported in the following years.

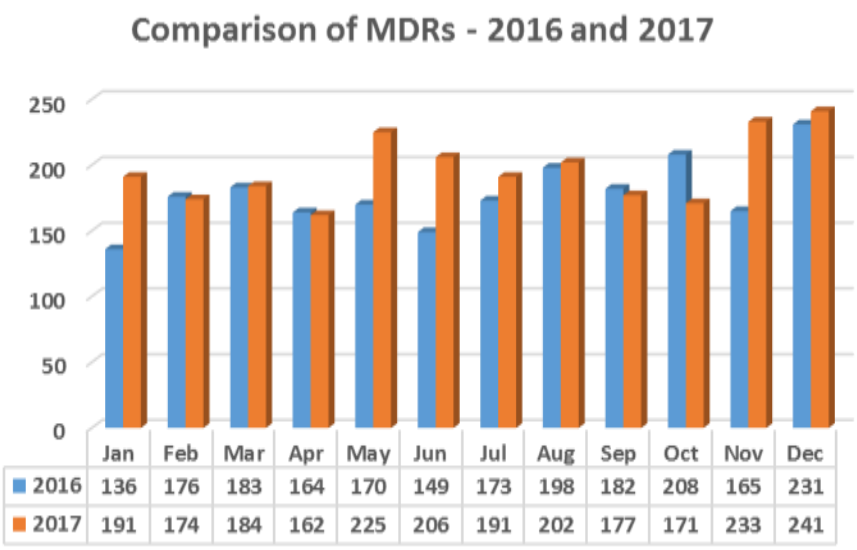

Figure 43. Comparison of MDR events reported in US for 2016 and 2017.

A Review of some of these reports provides an estimation of the actual risk based on the percentage of human errors. Some Draeger Medical Systems, Inc. and Shenzhen Mindray Bio-Medical Electronics CO. LTD. MDRs were reviewed.

As discussed above, the total number of adverse events in delivering anesthesia are mainly caused by factors that do not involve anesthesia machines. An accurate analysis was performed for 13 events, and it was found that the devices performed according to the manufacturer's specifications in almost all the circumstances, and external factors were responsible for the failures (L. Dinia, 2018). In three of these adverse events, the conditions of the patients were already very critical before the beginning of the procedure with severe pulmonary diseases, pulmonary HTN, and swings in heart rate and blood pressure. For these three cases, there were no signs of malfunctioning of the machines, but the critical conditions of the patients and the risk of negative consequences during and after the surgery increased the caregiver's perception of risk, therefore possibly blaming the machines for unrealistic failures. A further high-risk event was reported when smoke was coming out of a machine before it was used on a patient. In this case, an investigation by Mindray DS USA, Inc. showed traces of liquid on top of the machine with the liquid entering the device making contact with the electronic parts. The outcome for the hospital personnel would have been tragic because of negligence or carelessness. In another adverse event reported, the patient was bagged manually from the anesthetist for the entire duration of the surgery. The customer stated that the device was delivering low volume during automatic ventilation. It was discovered during the investigation that the customer did not follow the instructions on the absorbent canister and neither the

instructions on the wrap of the soda-lime absorbent, forgetting to remove the plastic wrap from the top of the part. Another event was related to a unit that did not work properly, which caused the automatic ventilation to stop, multiple doctors incurred in this accident. After the deep investigation, Draeger stated that the hospital needed just a deeper training and no malfunctions were confirmed.

In all the 13 events reviewed, the risk perceived by the caregiver was extremely high because of the consequences that the patients could have had (L. Dinia, 2018). During the adverse events, the caregiver perceived a high-risk due to a reduction of the controllability, an increase of the severity for the crucial timing in taking decisions, an altered communication due to status of stress, and a perception of failure of the device. All these factors contribute to an increase in the perception of risk tremendously. The proper investigations following the events showed that for 12 out of 13 events the root cause was the human error. The events were caused by improper behavior/distraction or very critical conditions of the patients before the cases.

A.9 Discussion on the Improvements

From an analysis of the MDR events, a tremendous educational value can be achieved for the manufacturers and the hospital personnel in order to find preventative and corrective measures to improve patient safety. After reviewing the data, it can be evaluated if design changes on the devices may be necessary or if a different and longer training needs to be offered to the caregivers. Unfortunately, even though the potential of collecting complaints is known, many clinical personnel lack to report complications because of the sense of fear or guilt coming from the other colleagues (A.F. Smith, 2006). In this context, the work of the manufacturer is crucial in training the caregiver on the use of the machines, but also in raising awareness of the importance of reporting events to improve the work quality of anesthesiologists and to increase patient safety. When either an emerging or recurring issue is identified from a manufacturer after the investigation, a risk assessment is required. The risk is assessed to understand if actions have to be taken only to improve the performance and the quality of the device or any corrective actions should be taken because the risk needs to be reduced for the public health. From the analysis of the adverse events for 2017, it was found that the human error was almost the only root cause, showing sometimes negligence, improper behaviors and carelessness from the caregiver (L. Dinia, 2018). Also, the lack of familiarity with the anesthesia machine is a source of errors, because of the perception of not being completely in

control of the equipment. These two aspects can be improved with new methods of training, reducing the perception of risk in delivering anesthesia.

Assigning an arbitrary number to the anesthetic risk that has a general application does not meet the clinical needs. Since the first procedures, anesthesiologists felt the duty to give a numerical evaluation of the risk that a specific case could have had for a patient. In this context, the first scores were created with a 1 to 3 scale for the importance of the case and from 1 to 3 depending on the conditions of the patient (G. Bellucci, 1990). The two scores were summed obtaining a value between 2 and 6 that still has the task to express a risk factor (G. Bellucci, 1990).

According to previous studies, people with strong initial opinions are hard to change their ideas, even in presence of evidences (P. Slovic, 1987). This behavior depends on how the information is interpreted (P. Slovic, 1987). One innovative way of presenting the same information about risk is to reinforce positive statements to alter people's attitude and perception, as for example showing the survival rates instead of the mortality rates (P. Slovic, 1987). In the last years, many engineering improvements have been made on anesthesia machines to prevent human errors; for instance, on the manufacturing of the cylinder or gas hoses with specific keys in order to avoid the connection at the wrong place. All these technological solutions have the purpose to improve patient safety through a reduction of errors.

One of the causes of errors that can have an important effect on the perception of the risk is the physical and mental condition that the clinicians and anesthesiologists have while practicing. When the medical operators are under fatigue, illness or stress (D.M. Gaba, 2000) the risk could increase, affecting the final performance of the procedure, reducing the patient safety. Sometimes, indeed, the caregiver is forgetful or distracted during the set-up phase of the device and this can negatively impact the good outcome of the procedure. Nowadays, the anesthesia machines have several automatic preliminary tests that can help the work of the clinicians, but at the same time errors can be made skipping some of these fundamental leak tests. As discussed in the previous section, some operations have to be done by the clinicians manually, like removing the plastic cover on the soda-lime absorbent for the CO2 before installing in the same machine. Even if there are clear labels on the part and on the machine, the risk to make errors is around the corner. A solution for the reduction of human errors can be provided with the use of checklists (B.D. Winters, 2009). Anytime during the start-up phase, the operator responsible for the functional checks should be filling a detailed checklist, signing the final report. This measure would reduce the opportunity to make errors due to distractions, lack of following the procedures properly, and wrong initiatives due to

different attitude and perception. Even though the checklists have a great potential to reduce risks and to improve safety, they are underused (B.D. Winters, 2009) for different reasons. A great improvement in delivering anesthesia can be made by a specific training through the simulations of real cases (P. Dalley, 2004). Many studies showed that hospital personnel learns much more during emergencies and unexpected events than during routine cases. The confidence and the knowledge of the anesthesiologists can be improved during the simulation to lead to a deeper understanding of how the device works, and thus to be more reactive in the potential adverse situations (P. Dalley, 2004). A further factor that increases the perception of risk in anesthesia is the use of non-recommended and aggressive cleaning solutions to prevent that germs and bacteria spread out and create infections. Often this behavior affects the quality and the performances of devices because during the pre-market test only a specific range of cleaners and disinfectants are approved. The result is a reduction of the reliability of the devices, increasing the perception of risk. The use of appropriate labels and even marks directly on the chassis of the devices may help to discourage the use of non-recommended cleaning agents and to educate hospital personnel. From the analysis of the adverse events reported, the episode with smoke coming out of a machine provides hints on the importance of education. Negligence, incompetence, and carelessness are often responsible for adverse events. Greater responsibility and common sense could be increased with courses in which basic concepts, combined with graphic examples of the consequences, are explained.

According to the Institute of Medicine (IOM), an excellent system of care delivery centers the emphasis on the main aspects of preventing errors, learning from the errors that do occur, and is built on a culture of safety that involves a collective approach by health-care professionals, organizations, and patients (P. Aspden, 2004). Manufacturers play a key role in improving the quality of the care delivered. The IOM defines patient safety as “the prevention of harm to patients” (P. Aspden, 2004).

According to the IOM: “the biggest challenge to moving toward a safer health system is changing the culture from one of blaming individuals for errors to one in which errors are treated not as personal failures, but as opportunities to improve the system and prevent harm” (Institute of Medicine (US), 2001).

A.10 Conclusion

The direct contact between the patient and the anesthesiologist, before the procedure, is an essential step to assure an optimal final outcome of the anesthetic

procedure. Even though the perception of the risk is often magnified because of factors as distractions, lack of confidence in using the equipment, and miscommunication between the hospital personnel just to cite few, the supervision of the anesthesiologist is fundamental to reduce the actual risk, avoiding adverse events due to the misuse of anesthesia machine or error in the clinical procedure which together are more than 80% of the total incidents. The comparison between the MDRs reported in 2016 and 2017 showed a growth trend suggesting a tendency of an increasing number of MDRs reported in the following years also due to a market growth. The analysis in this paper showed that the perceived risk of the hospital personnel is usually higher than the actual risk quantified through the quality management system by the manufacturers.

Appendix B - Effect on the Balance from Patellar Taping

The estimation of Centre of Mass trajectory (CoM) is a research topic of interest in human biomechanics. Human motion stability during both walking and standing is strictly related to CoM displacement (H.-J. Lee; D. A. Winter, 1995). CoM is defined as a point in which the whole body weight is equally balanced in all directions, and the resulting moment produced by all body-segments is null.

The Center of pressure (CoP), instead, is the application point of the ground reaction forces under the feet. Falls occur when CoM displacement exceeds feet' support base (CoM-SB) (D. A. Winter, 1995; M. Fujimoto, 2015). In fact, as CoM-SB provides a possible area for CoP movement, its boundaries have been considered as the stability limits within human balance is maintained (M. Fujimoto, 2015). After an external perturbation, several postural strategies are adopted to rapidly move the CoP in order to maintain CoM inside COM-SB. Protective steps, appropriately timed and adjusted, and hip and/or ankle movements are the common postural strategies adopted to adjust the CoM displacement as a function of perturbation intensity. It has been demonstrated that the assessment of CoM has great potential to estimate rehabilitation improvement on postural stability, discriminate between faller and non-faller and monitoring the balance dysfunction occurring with aging (E. Yu).

Motion capture systems and force platforms are still the best technologies for the estimation of accurate CoM measurements. Based on those technologies, several methods have been proposed over the last decade. More specifically, CoM can be assessed (D. Lafond, 2004) as: (i) displacement of weighted body-segments; (ii) single body displacement; and, (iii) double-integration of horizontal ground reaction force.

However, limitations of traditional instrumentation, such as the high cost, the limited indoor environment, requirements for skilled operator's supervision, are fueling the development of novel methods through wearable technologies suitable for the real-time home monitoring. In the last few years, different methods based on inertial sensors

systems have been proposed based on the double integration of acceleration signals of pelvis-worn sensors (M. J. Floor-Westerdijk, 2012).

More, specifically, the BM will be fed with 3D motion analysis data from inertial sensors placed on body-segments. It is based on a body-segments' kinematics chain, a Functional Calibration (FC) procedure and anthropometric data (E. Palermo, 2014). By means of these assumptions, the kinematics joint angles and spatio-temporal parameters have been demonstrated to be accurately measured in ambulatory setting (A. Pacilli, 2016). However, the accuracy of the BM in the CoM assessment is still untapped.

Among the several possible applications, this new method could provide important information on the correlation between the patella taping and the neuromuscular control; the patellar taping technique through the medialization of the patella (J. McCONNELL, 1986) allows subjects to engage in pain-free physical therapy exercises. This method has been already investigated, showing a reduction of the perceived pain of the patients with patellofemoral pain syndrome with the consequent improvement of the neuromuscular activities (N. Aminaka and P. A. Gribble, 2008); a wider study on how the patellar tape influences the postural stability thought CoM assessment could have important implications in the long term management of Chondromalacia Patellae.

The proposal for this study was sent to the *Department of Mechanical and Aerospace Engineering, Sapienza University,* to collaborate on the execution of the research program. The patellar taping technique proposed by Mulligan has already been investigated in the past on patients that were affected by subacute stroke. 30 patients were observed during static and dynamic trials. The patients were divided into two groups of 15 each, the first group received the Mulligan taping while the second had a placebo taping. It was observed that the patients with the Mulligan taping had a balance and gait analysis improvements (K.H. Hyun, 2015).

In 2011 a study was conducted by Seyit Citaker in which it was tried to define a correlation between "one-leg static standing balance" (OLSSB) and "patellofemoral pain syndrome" (PFPS). The initial hypothesis of the study was that the "one-leg static standing balance" decreased in patients affected by "patellofemoral pain syndrome". In conclusion, the research showed that the OLSSB depended mainly on the quad muscle and on the ischiocrural muscles, while correlations between OLSSB and pain, Q angle, and "lower extremity alignment" were not observed (S. Citaker, 2011). A relationship between the static balance and the "patellofemoral syndrome" was shown in the research conducted by Seyit Citaker. The conclusion of the study was that the symptomatic side performed worse than the asymptomatic side; most likely the authors' idea was based on the use of the taping to reduce the pain, improving the static balance.

After this study, it was thought to investigate the static and dynamic balances for a normal subject with the same taping. Moreover, it was speculated about how the patella taping impacts the balance during a dynamic functional test.

The correlation between the McConnel taping and the loss of balance on healthy subjects and subjects with "patellofemoral syndrome" would be very interesting to analyze. In 2008 the researchers of Toledo were the first to start to investigate the taping's effect on the patella during a dynamic postural control exercise. The study confirmed that the patella taping reduced the pain in the subjects with PFPS and improved the performance during the "Star Excursion Balance Test" (SEBT). The clinical reasons of these results are still under investigation. At the end of the study, it was evident that a further research was necessary to better understand the role of the patella taping on the neuro-muscular system during a dynamic postural control (N. Aminaka and P. A. Gribble, 2008).

Therefore, the aim of this project will be pursued thought static and dynamic tasks performed twice both by healthy subjects and not-healthy ones, with and without patellar tape, simultaneously gathered from both optoelectronic systems and inertial sensors.

The further clinical tests will involve, beyond 20 healthy subjects, also subjects with patellofemoral syndrome and subjects with neurological deficit as well. All the demographic data will be collected during the trials. The static and dynamic trials will be carried out on the subjects as follows:

- Single foot position standing for 30 seconds
- Bipodalic position standing for 30 seconds
- Walking test
- Bipodalic position with different movements of the hip
- Bipodalic position and squat
- "Cone taps – single leg stance" (Figure 44)

Figure 44. "Cone taps – single leg stance". During the trial, a tennis ball and 5 cones are used.

The study was the result of my intuition about how the patella position could have an impact on the subject balance, which is regulated by the visual, vestibular, and proprioceptive systems in the human beings. This research project has many variants that can be studied and developed like, for instance, the same study conducted with open or closes eyes.

The results that could be obtained during the study could lead to interesting theories in which some subjects with specific deficiencies will show improvements in their performances with the use of McConnel taping. During the study there will be several questions that will need to be answered such as, for instance: does the tape make the subjects safer because of the placebo effect? Is there an improvement of the performance because the subjects feel less pain? Is there a change in the sensorial input that has an impact on the performance?

Conclusion

In the first two chapters, innovative optical sensors have been developed with applications in the preservation and conservation of archaeological sites, monuments and artworks. The FBG sensor for monitoring the pH of the rain was miniaturized with respect to many sensors present in literature and it was also able to reach, through simulations, sensitivity values up to 8.58 nm/pH in the pH range 4-7.1. The pH range 4-7.1 was chosen for the study because the acid rain assumes on average pH values within this range and the value 4 is the minimum value that the acid rain, usually, assumes in the archeological areas and where the artworks are located. Moreover, it was relevant to show the behavior of the sensor in a range between a value immediately higher than the neutral pH and one of the minimum values of the acid rain that affects the artworks in order to consider all intermediate scenarios. Another main reason why this range was also considered is because the hydrogel that is surrounding the fiber shows a strain uniformly distributed within it. This provides a linear response of the sensor. Monitoring the pH of the rain in contact with artworks leads to predicting and controlling the corrosion of specific materials, especially limestone and marble, thus scheduling timely restoration.

The tag recognition method developed is a measurement system with which it is possible to determine displacements between two or more tags of the order of ten micrometers at a camera-tags distance of 25 cm and with a relative error lower than 3%. The performance, and thus the resolution, of the methodology could be increased both by reducing the distance between the acquisition system and the target, and increasing the camera's resolution. It was observed that this methodology can be adequately used for SHM, in particular, to monitor cracks of Cultural Heritage without buildings invasiveness.

In the second part of the Ph.D., a research in the biomedical field was conducted. First the risk and the perception of risk related to anesthesia delivery was studied. The difference was analyzed between the actual risk, defined by numerical values as intended by the medical devices manufacturers, and the perception of the risk commonly subjectively interpreted by the hospital personnel and influenced by several factors with high variability. In conclusion, it was shown that, usually, the perception of the risk for the hospital personnel is higher than the actual risk, and, through different strategies, it could be mitigated, providing a higher level of patient safety.

In the end, a biomechanical study was proposed for deeper investigating the correlation between the patellar taping introduced by McConnell and the neuromuscular control.

List of Publications and Awards

Magazine publications

[1] Fabio Mangini, Livio D'Alvia, Mauro Del Muto, Lorenzo Dinia, Enrico Federici, Eduardo Palermo, Zaccaria Del Prete, and Fabrizio Frezza, "Tag recognition: A new methodology for the structural monitoring of cultural heritage," Measurement, 127, pp. 308-313, 2018.

[2] Lorenzo Dinia, Fabio Mangini, Marco Muzi, and Fabrizio Frezza, "FBG Multifunctional pH Sensor - Monitoring the pH Rain in Cultural Heritage," Acta Imeko, 7(3), pp. 24-30, 2018, ISSN: 2221-870X.

[3] Lorenzo Dinia, Fabio Mangini, Maria Alessandra Marella, and Fabrizio Frezza, "Parallelism between Risk and Perception of Risk among Caregivers during Anesthesia Delivery," (submitted).

Congress proceedings

[1] L. Dinia, F. Mangini, M. Muzi, F. Frezza, "Fiber Bragg grating multifunctional pH sensor for monitoring the rain in cultural heritage," in: IMEKO International Conference on Metrology for Archaeology and Cultural Heritage, at Lecce, Italy, 2017, pp. 213-216, ISBN: 978-1-5108-5818-3.

[2] F. Mangini, Lorenzo Dinia, F. Frezza, A. Beccarini, M. Del Muto, E. Federici, S. Godi, and A. Segneri, "New crack measurement methodology: Tag Recognition," in: IMEKO International Conference on Metrology for Archaeology and Cultural Heritage, at Lecce, Italy, 2017.

[3] L. Dinia, F. Mangini, and F. Frezza, "Can the Perception of Risk Be Decreased among Caregivers during Anesthesia Delivery?," in: IEEE International Symposium on Medical Measurements and Applications (MeMeA), at Rome, Italy, 2018.

[4] F. Mangini, C. Cantisani, L. Dinia , F. Cantoresi, F. Ponti, R. Marino, P. Simeoni, M. Troiano, and F. Frezza, "Machine learning monitoring of skin moles and skin-cancer detection," 24th world congress of dermatology, Milan, 2019 (submitted).

Awards

[1] Lorenzo Dinia, Fabio Mangini, "FBG Sensore di pH multifunzionale – Monitoraggio del pH della pioggia applicato ai Beni Culturali," Vincitore Premio Marabelli – I Giovani e l'Innovazione Scientifica, Museo Nazionale Etrusco di Villa Giulia (Roma), 24 Ottobre 2018.

References

A. Macchia F. Mangini, S. A. Ruffolo, M. Muzi, L. Rivaroli, M. Ricca, F. Frezza A novel model to detect the content of inorganic nanoparticles in coatings used for stone protection [Journal] // Progress in Organic Coatings. - 2017. - Vol. 106. - pp. 177-185.

A. Pacilli I. Mileti, M. Germanotta, E. DI Sipio, I. Imbimbo, I. Aprile, L. Padua, S. Rossi, E. Palermo, and P. Cappa, A Wearable Setup for Auditory Cued Gait Analysis in Patients with Parkinson's Disease [Conference] // IEEE International Symposium on MeMeA, Proceedings in Press. - 2016.

A. Saisi M. Guidobaldi, C. Gentile On site investigation and health monitoring of a historic tower in Mantua [Journal]. - [s.l.] : Appl. Sci., 2016. - 173 : Vol. 6. - p. 18.

A. Singh M. Agrawal Acid rain and its ecological consequences [Journal] // Journal of Environmental Biology. - 2008. - 1 : Vol. 29. - pp. 15-24.

A.F. Smith D. Goodwin, M. Mort, and C. Pope Adverse events in anaesthetic practice: qualitative study of definition, discussion and reporting [Journal] // British Journal of Anaesthesia. - 2006. - 6 : Vol. 96. - pp. 715-721.

A.M. Adams and A.F. Smith Risk perception and communication: recent developments and implications for anesthesia [Journal]. - [s.l.] : Anaesthesia, 2001. - 8 : Vol. 56. - pp. 745-755.

B.D. Winters A.P Gurses, H. Lehmann, J.B. Sexton, C.J. Rampersad, and P.J. Pronovost Clinical review: checklists - translating evidence into practice [Journal] // Critical Care. - 2009. - 6 : Vol. 13. - p. 210.

C. Gentile M. Guidobaldi, A. Saisi A One-year dynamic monitoring of a historic tower: damage detection under changing environment [Journal]. - [s.l.] : Meccanica, 2016. - 11 : Vol. 51. - pp. 2873–2889.

C.F. Carlborg K.B. Gylfason, A. Ka mierczak, F. Dortu, M.J.B. Polo, A.M. Catala, G.M. Kresbach, H. Sohlström, T. Moh, and L. Vivien A packaged optical slot-waveguide ring resonator sensor array for multiplex label-free assays in labs-on-chips [Journal] // Lab Chip. - 2009. - Vol. 10. - pp. 281-290.

C.F. Swinhoe and E.R. Groves Patients' Knowledge of Anaesthetic Practice and the Rôle of Anaesthetists [Journal] // Anaesthesia. - 1994. - 2 : Vol. 49. - pp. 165-166.

Comsol Application License 5.2 Optical Ring Resonator Notch Filter. - [s.l.] : Comsol Multiphysics 5.2.

D. A. Winter Human balance and posture control during standing and walking [Journal]. - 1995. - Vol. 3. - pp. 193–214.

D. C. S. Summers Quality [Book]. - [s.l.] : Pearson Education, Inc., 2006. - 4.

D. Camuffo Acid Rain And Deterioration Of Monuments: How Old Is The Phenomenon? [Journal] // Atmospheric Environment. - 1992. - 2 : Vol. 26B.

D. Lafond M. Duarte, and F. Prince, Comparison of three methods to estimate the center of mass during balance assessment [Journal]. - [s.l.] : J. Biomech, 2004. - 9 : Vol. 37. - pp. 1421–1426.

D. Marquardt An algorithm for least-squares estimation of nonlinear parameters [Journal]. - [s.l.] : SIAM J. Appl. Math. 11, 1963. - pp. 431–441.

D.G. Rabus Integrated Ring Resonators [Book]. - [s.l.] : Springer, 2007.

D.J. Malenka J.A. Baron, S. Johansen, J.W. Wahrenberger, and J.M. Ross The framing effect of relative and absolute risk [Journal] // Journal of General and Internal Medicine. - 1993. - 10 : Vol. 8. - pp. 543-548.

D.M. Gaba Anaesthesiology as a model for patient safety in health care [Journal]. - [s.l.] : British Medical Journal, 2000. - 7237 : Vol. 320. - pp. 785-788.

E. Palermo S. Rossi, F. Marini, F. Patanè, and P. Cappa, Experimental evaluation of accuracy and repeatability of a novel body-to-sensor calibration procedure for inertial sensor-based gait analysis [Journal]. - [s.l.] : Meas. J. Int. Meas. Confed., 2014. - 1 : Vol. 52. - pp. 145–155.

E. Yu M. Abe, K. Masani, N. Kawashima, F. Eto, N. Haga, K. Nakazawa, and A. E. Yu, Evaluation of Postural Control in Quiet Standing Using Center of Mass Acceleration: Comparison Among the Young, the Elderly, and People With Stroke [Journal].

F. Farahi D.J. Webb, J.D.C. Jones, and D.A. Jackson Simultaneous Measurement of Temperature and Strain: Cross-Sensitivity Considerations [Journal] // Journal of Lightwave Technology. - 1990. - 2 : Vol. 8. - pp. 138-142.

F. Mangini F. Frezza, A. Beccarini, M. Del Muto, E. Federici, S. Godi, A. Segneri, New crack measurement methodology: Tag Recognition [Conference]. - Lecce : IMEKO International Conference on Metrology for Archaeology and Cultural Heritage, 2017.

F. P. Branca Fondamenti di Ingegneria Clinica [Book]. - MIlano : Springer-Verlag Italia, 2002. - Vol. 1.

G. Bellucci G. Damia, and A. Gasparetto In Trattato Enciclopedico di Anestesia, Rianimazione e Terapia Intensiva [Book] / ed. Piccin ed.. - [s.l.] : Nuova Libreria, 1990. - Vol. 2: Anestesiologia generale.

G. C. Righini Y. Dumeige, P. Feron, M. Ferrari, G. Nunzi Conti, D. Ristic, and S. Soria Whispering gallery mode microresonators: Fundamentals and applications [Journal] // Rivista del nuovo Cimento. - 2011. - 7 : Vol. 34.

G.C. Heard P.M. Sanderson, and R.D. Thomas Barriers to adverse event and error reporting in anesthesia [Journal] // Anesthesia & analgesia. - 2012. - 3 : Vol. 114. - pp. 604-614.

G.E. Likens F.H. Bormann, and N.M. Johnson Acid Rain [Journal] // Environment: Science and Policy for Sustainable Development. - 2008. - 2 : Vol. 14. - pp. 33-40.

H. Li Smart Hydrogel Modelling [Conference]. - Berlin : Springer, 2009.

H. Li T.Y. Ng, Y.K. Yew, and K.Y. Lam Modeling and simulation of the swelling behavior of pH-stimulus-responsive hydrogels [Journal] // Biomacromolecules. - 2004. - Vol. 6. - pp. 109-120.

H.-J. Lee and L.-S. Chou Detection of Gait Instability Using the Center of Mass and Center of Pressure Inclination Angles.

H.K. Cho and J. Han Numerical Study of Opto-Fluidic Ring Resonators for Biosensor Applications [Journal] // Sensors. - 2012. - Vol. 12. - pp. 14144-14157.

H.W. Cho H.J. Yoon, J.C. Yoon Analysis of crack image recognition characteristics in concrete structures depending on the illumination and image acquisition distance through outdoor experiments [Conference]. - [s.l.] : Sensors, 2016. - Vol. 16. - p. 21.

I. Yulianti A.S.M. Supa'at, S.M. Idrus, O. Kurdi, and M.R.S. Anwar Modeling of hydrogel coated fiber Bragg grating pH sensor [Journal] // International Journal of Information and Electronics Engineering. - 2013. - 3 : Vol. 3. - pp. 99-103.

I. Yulianti A.S.M. Supa'at, and S.M. Idrus Characterization of fiber Bragg grating sensor for pH measurement [Conference] // Advanced Intelligent Mechatronics (AIM), IEEE/ASME International Conference on. - Besancon, France : [s.n.], 2014. - pp. 1163-1166.

I. Yulianti A.S.M. Supa'at, S.M. Idrus, N.M. Kassim, and A.M. Al-hetar Fiber Bragg grating based pH sensor [Conference] // Enabling Science and Nanotechnology (ESciNano), International Conference on. - Kuala Lumpur, Malaysia : [s.n.], 2010. - pp. 424-428.

Industry Experts Anesthesia Devices – A Global Market Overview [Book]. - [s.l.] : Industry Experts, 2013.

Institute of Medicine (US) Crossing the quality chasm: a new health system for the 21st century. - [s.l.] : Washington DC: National Academy Press (US), 2001. - p. 8.

J. Garcia-Palacios J.M. Soria, I.M. Díaz, F. Tirado-Andrés Modal tracking with only a few of sensors: Application to a residential building [Conference] // 8th European Workshop on Structural Health Monitoring. - [s.l.] : EWSHM 2016, 2016.

J. McCONNELL The Management of Chondromalacia Patellae: A Long Term Solution [Journal] // Aust. J. Physiother.. - 1986. - 4 : Vol. 32. - pp. 215-223.

J.B. Cooper R.S. Newbower, C.D. Long, and B. McPeek Preventable Anesthesia Mishaps: A study of human factors* [Journal] // Quality and Safety in Health Care. - 2002. - 3 : Vol. 11. - pp. 277–282.

J.E. Dennis Jr. Nonlinear least-squares, State of the art in numerical analysis [Journal] / ed. Jacobs D.. - London : Academic Press, 1977. - pp. 269-312.

J.J. Moré The Levenberg-Marquardt algorithm: implementation and theory, numerical analysis [Book Section] // Lecture Notes in Mathematics / ed. Watson G.A.. - [s.l.] : Springer Verlag, 1977.

J.P. Bagian C. Lee, J. Gosbee, J. DeRosier, E. Stalhandske, N. Eldridge, R. Williams, and M. Burkhardt Developing and deploying a patient safety program in a large health care delivery system: you can't fix what you don't know about [Journal] // Jt Comm J Qual Improv. - 2001. - 10 : Vol. 27. - pp. 522-532.

J.P. Haberer Consultation Préanesthésique [Book]. - [s.l.] : Encyclopédie Médico-Chirurgical, 2001.

K. Levenberg A Method for the Solution of Certain Problems in Least-Squares [Journal]. - [s.l.] : Q. Appl. Math. 2, 1944. - pp. 164-168.

K.H. Hyun H.Y. Cho, and C.G. Lim, The effect of knee joint Mulligan taping on balance and gait in subacute stroke patients [Journal]. - [s.l.] : J. Phys. Ther. Sci., 2015. - Vol. 27. - pp. 3545–3547.

L. Dinia F. Mangini, and F. Frezza Can the Perception of Risk Be Decreased among Caregivers during Anesthesia Delivery? [Conference] // IEEE International Symposium on Medical Measurements and Applications (MeMeA). - Rome : [s.n.], 2018.

L. Dinia F. Mangini, M. Muzi, and F. Frezza Fiber Bragg grating multifunctional pH sensor for monitoring the rain in cultural heritage [Conference] // IMEKO International Conference on Metrology for Archaeology and Cultural Heritage. - Lecce, Italy : [s.n.], 2017. - pp. 213-216.

L. Dinia F. Mangini, M. Muzi, F. Frezza Fiber Bragg Grating Multifunctional pH Sensor for Monitoring the rain in Cultural Heritage [Conference]. - Lecce : IMEKO International Conference on Metrology for Archaeology and Cultural Heritage, 2017.

L. Zhou X. Sun, X. Li, and J. Chen Miniature Microring Resonator Sensor Based on a Hybrid Plasmonic Waveguide [Journal] // Sensors. - 2011. - Vol. 11. - pp. 6856-6867.

L.Y. Shao M.J. Yin, H.Y. Tam, and J. Albert Fiber optic pH sensor with self-assembled polymer multilayer nanocoatings [Journal] // Sensors. - 2013. - Vol. 13. - pp. 1425-1434.

M. Baskar Rao M.R. Bhat, C.R.L. Murthy, K. Venu Madhav, S. Asokan, Structural Health Monitoring (SHM) Using Strain Gauges, PVDF Film and Fiber Bragg Grating (FBG) Sensors:

A Comparative Study [Conference]. - Hyderabad : National Seminar on Non-Destructive Evaluation, 2006.

M. Belavic M. Lončarić-Katušin, and J. Žunić Reducing the incidence of adverse events in anesthesia practice [Journal] // Periodicum Biologorum. - 2013. - 2 : Vol. 115. - pp. 145-148.

M. Debliquy J.-M. Renoirt, C. Caucheteur, P. Mégret, and M.-G. Olivier, PH sensor based on tilted fiber Bragg gratings covered by a sol-gel [Conference] // The 14th International Meeting on Chemical Sensors. - Nuremberg : IMCS 2012, 2012. - pp. 652-654.

M. Fujimoto W.-N. Bair, and M. W. Rogers Center of pressure control for balance maintenance during lateral waist-pull perturbations in older adults [Journal]. - [s.l.] : J. Biomech, Apr 2015. - 6 : Vol. 48. - pp. 963–8.

M. J. Callaghan J. Selfe, A. McHenry, and J. A. Oldham Effects of patellar taping on knee joint proprioception in patients with patellofemoral pain syndrome [Journal] // Man. Ther.. - [s.l.] : Man. Ther., 2008. - 3 : Vol. 13. - pp. 192-199.

M. J. Floor-Westerdijk H. M. Schepers, P. H. Veltink, E. H. F. Van Asseldonk, and J. H. Buurke Use of inertial sensors for ambulatory assessment of center-of-mass displacements during walking [Journal] // IEEE Trans. Biomed. Eng.. - 2012. - 7 : Vol. 59. - pp. 2080–2084.

M. J. Floor-Westerdijk H. M. Schepers, P. H. Veltink, E. H. F. Van Asseldonk, and J. H. Buurke, Use of inertial sensors for ambulatory assessment of center-of-mass displacements during walking [Journal]. - [s.l.] : IEEE Trans. Biomed. Eng.. - 7 : Vol. 59. - pp. 2080–2084.

M.F. Jaafar H.M. Saman, and M.N.M. Sidek Simultaneous monitoring on corrosion-pH-temperature using multiplexed fiber Bragg grating sensors techniques in new RC structure: A Review [Journal] // International Journal of Civil Engineering and Geo-Environmental. - 2013. - Vol. 4. - pp. 41-48.

M.-G. Masciotta J.C.A. Roque, L.F. Ramos, P.B. Lourenço A multidisciplinary approach to assess the health state of heritage structures: the case study of the Church of Monastery of Jerónimos in Lisbon [Journal]. - [s.l.] : Constr. Build. Mater., 2016. - 30 : Vol. 116. - pp. 169–187.

M.J.P. Leiner and P. Hartmann Theory and practice in optical pH sensing [Journal] // Sensors and Actuators B: Chemical. - 1993. - Vol. 11. - pp. 281-289.

M.M. Werneck R.C.S.B. Allil, B.A. Ribeiro A Guide to Fiber Bragg Grating Sensors [Journal]. - [s.l.] : INTECH, 2013.

N. Aminaka and P. A. Gribble Patellar taping, patellofemoral pain syndrome, lower extremity kinematics, and dynamic postural control [Journal] // J. Athl. Train.. - 2008. - 1 : Vol. 43. - pp. 21-8.

N. Moerman F.S.A.M. Van Dam, and J. Oosting Recollections of General Anaesthesia: A survey of Anaesthesiological Practice [Journal] // Acta Anaesthesiologica Scandinavica. - 1992. - 8 : Vol. 36. - pp. 767-771.

N.A. Hoult M. Dutton, A. Hoag, W.A. Take Measuring crack movement in reinforced concrete using digital image correlation: overview and application to shear slip measurements [Journal]. - [s.l.] : Proc. IEEE, 2016. - 8 : Vol. 104. - pp. 1561–1574.

P. Aspden J.M. Corrigan, J. Wolcott, and S.M. Erickson Patient safety: achieving a new standard for care [Journal]. - [s.l.] : Washington DC: National Academies Press (US), 2004.

P. Dalley B. Robinson, J. Weller, and C. Caldwell The use of high-fidelity human patient simulation and the introduction of new anesthesia delivery system [Journal] // Anesth Analg. - 2004. - 6 : Vol. 99. - pp. 1737-1741.

P. Slovic and E. Peters Risk Perception and Affect [Journal] // Psychological Science. - 2006. - 6 : Vol. 15. - pp. 322-326.

P. Slovic E.U. Weber Perception of Risk Posed by Extreme Events [Conference] // Risk Management Strategies in an Uncertain World conference. - Palisades, New York : [s.n.], 2002.

P. Slovic Perception of Risk [Journal] // Science. - 1987. - Vol. 236. - pp. 280-285.

P.M. Osswald O. Swars, and P. Levfke 10 Scores, Scorning and Outcome: Correlation between Preoperative Assessment and Post-Operative Morbidity and Mortality of non-Hospitalized and Hospitalized Patients [Journal] // International Journal of Surgery. - 1998. - 3 : Vol. 12. - pp. 471-483.

R. Butlin Effects of Air Pollutants on Buildings and Materials [Conference] // Proceedings of the Royal Society of Edinburgh. Section B. Biological Sciences. - 1990. - Vol. 97. - pp. 255-272.

R. Ceravolo A. De Marinis, M.L. Pecorelli, L.Z. Fragonara Monitoring of masonry historical constructions: 10 years of static monitoring of the world's largest oval dome [Conference]. - [s.l.] : Struct. Control Health Monitoring, 2017. - Vol. 24. - p. 11.

R. Gotti Microrisonatori Ottici Fabbricati Mediante Polimerizzazione A Due Fotoni. - [s.l.] : Politecnico di Milano, 2013.

R. Suszynsk K. Wawryn Stars' centroid determination using PSF-fitting method [Journal]. - [s.l.] : Metrol. Measure. Syst., 2015. - 4 : Vol. 22. - pp. 547-558.

R.J. Cheng J.R. Hwu, J.T. Kim, and S.M. Leu Deterioration of Marble Structures. The Role of Acid Rain [Journal] // Analytical Chemistry. - 1987. - 2 : Vol. 52. - pp. 104A-106A.

S. Citaker D. Kaya, I. Yuksel, B. Yosmaoglu, J. Nyland, O.A. Atay, and M.N. Doral, Static Balance in Patients With Patellofemoral Pain Syndrome [Journal]. - [s.l.] : Sports Physical Therapy, 2011.

S. Roh T. Chung, B. Lee Overview of the characteristics of micro-and nano-structured surface plasmon resonance sensors [Journal] // Sensors. - 2011. - Vol. 11. - pp. 1565-1588.

S.J. Haneef J.B. Johnson, C. Dickinson, G.E. Thompson, and G.C. Wood Effect of Dry Deposition of NOx and SO2 Gaseous Pollutants on the Degradation of Calcareous Building Stones [Book]. - [s.l.] : Atmospheric Environment. Part A. General Topics, 1992. - Vol. 26 : 16 : pp. 2963-2974.

T. Claes J. G. Molera, K. De Vos, E. Schacht, R. Baets, and P. Bienstman Label-free biosensing with a slot-waveguide-based ring resonator in silicon on insulator [Journal] // IEEE Photon. J.. - 2009. - Vol. 1. - pp. 197-204.

T. Delabiey J. De Schutterz, B. Vandenbussche An accurate and efficient gaussian fit centroiding algorithm for star trackers [Journal]. - [s.l.] : J. Astronautical Sci., 2014. - 1 : Vol. 61. - pp. 60-84.

T. Walsh and P.C.W. Beatty Human factors error and patient monitoring [Journal] // Physiological Measurement. - 2002. - 3 : Vol. 23. - pp. R111-132.

T. Wu Y. Liu, Z. Yu, Y. Peng, C. Shu, and H. Ye The sensing characteristics of plasmonic waveguide with a ring resonator [Journal] // Optics Express. - 2014. - 7 : Vol. 22.

T.P. Jones and M.D. Porter Optical pH sensor based on the chemical modification of a porous polymer film [Journal] // Analytical Chemistry. - 1988. - Vol. 60. - pp. 404-406.

U.S. Food & Drug Administration Code of Federal Regulations Title 21 part 803. - 2016.

V. Gattulli M. Lepidi, F. Potenza Dynamic testing and health monitoring of historic and modern civil structures in Italy [Journal]. - [s.l.] : Struct Monitoring Maintenance, 2016. - 1 : Vol. 3. - pp. 71-90.

V.N.K. Pabbisetti and S.S. Madhuvarasu Hydrogel-coated fiber Bragg grating sensor for pH monitoring, [Journal] // Optical Engineering. - 2015. - 6 : Vol. 55. - pp. 066112-066112.

X. Chen C. Zhang, D.J. Webb, G.D. Peng , and K. Kalli Bragg grating in polymer optical fibre for strain, bend and temperature sensing [Journal] // Measurement Science and Technology. - 2010. - Vol. 21.

X. Fan I.M. White, S.I. Shopova, H. Zhu, J.D. Suter, and Y. Sun Sensitive optical biosensors for unlabeled targets: A review. [Journal] // Anal. Chim. Acta. - 2008. - Vol. 620. - pp. 8-26.

X.F. Huang Z.M. Chen, L.Y. Shao, K.F. Cen, D.R. Sheng, J.C., and H. Zhou Design and characteristics of refractive index sensor based on thinned and microstructure fiber Bragg grating [Journal] // Applied Optics. - 2008. - 4 : Vol. 47. - pp. 504-511.